Phase Change Memories in Smart Sensing Solutions for Structural Health Monitoring

Published Version:
Said Quqa, A.A. (2022). Phase Change Memories in Smart Sensing Solutions for Structural Health Monitoring. JOURNAL OF COMPUTING IN CIVIL ENGINEERING, 36(4), 1-13 [10.1061/(ASCE)CP.1943-5487.0001027].

Availability:
This version is available at: https://hdl.handle.net/11585/882025 since: 2022-05-27

Published:
DOI: http://doi.org/10.1061/(ASCE)CP.1943-5487.0001027

Phase change memories in smart sensing solutions for structural health monitoring

Said Quqa[1], Alessio Antolini[2], Eleonora Franchi Scarselli[3], Antonio Gnudi[4], Andrea Lico[5], Marcella Carissimi[6], Marco Pasotti[7], Roberto Canegallo[8], Luca Landi[9], Pier Paolo Diotallevi[10]

[1] PhD Student, DICAM – University of Bologna, Viale del Risorgimento 2, 40136 Bologna, Italy
said.quqa2@unibo.it
[2] PhD Student, DEI – University of Bologna, Viale del Risorgimento 2, 40136 Bologna, Italy
Research fellow, ARCES – University of Bologna, Viale Carlo Pepoli 3/2, 40125 Bologna, Italy
alessio.antolini2@unibo.it
[3] Associte Professor, DEI – University of Bologna, Viale del Risorgimento 2, 40136 Bologna, Italy
Associate Professor, ARCES – University of Bologna, Viale Carlo Pepoli 3/2, 40125 Bologna, Italy
eleonora.franchi@unibo.it
[4] Associte Professor, DEI – University of Bologna, Viale del Risorgimento 2, 40136 Bologna, Italy
Associate Professor, ARCES – University of Bologna, Viale Carlo Pepoli 3/2, 40125 Bologna, Italy
antonio.gnudi@unibo.it
[5] Research fellow, ARCES – University of Bologna, Viale Carlo Pepoli 3/2, 40125 Bologna, Italy
andrea.lico2@unibo.it
[6] R&D, STMicroelectronics, Via Camillo Olivetti 2, 20864 Agrate Brianza, Italy
marcella.carissimi@st.com
[7] R&D, STMicroelectronics, Via Camillo Olivetti 2, 20864 Agrate Brianza, Italy
marco.pasotti@st.com
[8] R&D, STMicroelectronics, Via Camillo Olivetti 2, 20864 Agrate Brianza, Italy
roberto.canegallo@st.com
[9] Associate Professor, DICAM – University of Bologna, Viale del Risorgimento 2, 40136 Bologna, Italy
l.landi@unibo.it
[10] Full professor, DICAM – University of Bologna, Viale del Risorgimento 2, 40136 Bologna, Italy
pierpaolo.diotallevi@unibo.it

Corresponding author: Said Quqa, e-mail: said.quqa2@unibo.it

Abstract

Smart devices for structural health monitoring provide edge computing capabilities to reduce wireless transmission and, thus, power consumption. Although effective algorithms have been proposed in the last few decades, traditional microcontrollers require heavy data flow between the memory and the central processing unit that involves a considerable fraction of the total energy consumption. Phase change memory has recently emerged as an attractive solution in the field of resistive non-volatile memory for analog in-memory computing, which is a valid approach to avoid data being conveyed among distinct elaboration units. However, it has never been envisaged in structural health monitoring applications. As this technology is still in an embryonic state, several challenges related to

nonlinearities and nonidealities of the memory elements and the energy expenditure related to the memory reprogramming process may undermine its usage. In this paper, the application of a novel identification approach for civil infrastructures is investigated using phase change memories. The main computational core of the presented algorithm, consisting of 1-dimensional convolutions, is particularly suitable for implementations involving analog in-memory computing, thus showing the great potential of this technology for structural health monitoring applications. The test unit is an embedded phase change memory provided by STMicroelectronics and designed in 90-nm smart power Bipolar-CMOS-DMOS technology with a Ge-rich Ge-Sb-Te alloy for automotive applications. Experimental results obtained for a viaduct of an Italian motorway support the efficacy of the method. Moreover, the influence of nonidealities on the outcomes of damage identification based on both dynamic and quasi-static structural parameters is examined.

Introduction

A considerable portion of civil infrastructure built in the last century is now close to, or even beyond, the end of its design lifespan. Besides, the traffic demand for ordinary viaducts and bridges is increasing and, in some cases, may overcome the design criteria.

Structural health monitoring (SHM) systems can be particularly helpful in assessing structural integrity to improve maintenance administration or post-disaster emergency management (Tan et al. 2020; Zonta et al. 2014). A considerable piece of research has been conducted lately to make vibration-based SHM techniques more and more advanced, dealing with the identification of structures with closely spaced vibration modes (Qu et al. 2018), operating with nonstationary excitation (Qu et al. 2019), and solving underdetermined problems with few recording channels (Yi et al. 2019). Also, recent procedures can identify or reconstruct complex modal parameters (Qu et al. 2021), which provide a complete picture of the monitored structure. Although vibration-based SHM is an established approach for the non-invasive evaluation of damage-sensitive features, traditional market sensing solutions employed in this field are generally expensive. Recently, low-cost sensing components, together with wireless transmission modules, have been studied to cut the costs related to the initial investment for an SHM system (Jo et al. 2012; Sabato et al. 2017). However, frequent battery replacement is not viable when the monitored structures are numerous and distributed over wide areas. For this reason, efficient algorithms and smart data management strategies are gaining growing interest in both research and field applications (Long and Büyüköztürk 2020; Noel et al. 2017).

Edge computing consists of accomplishing computation tasks onboard smart sensing nodes of a WSN, allowing data compression and transmitting shorter data streams. Since wireless transmission is particularly energy-demanding in wireless SHM systems, edge computing has recently proven to be an attractive solution (Hackmann et al. 2008; Jindal and Liu 2012; Long and Büyüköztürk 2020). Several studies have been conducted to adapt traditional identification techniques in distributed computing schemes (e.g., the frequency domain decomposition (Rice et al. 2011), the natural excitation technique (Jo et al. 2012), and the random decrement method (Sim et al. 2011)), involving smart sensors organized in tree-type computational models. More recently, Long and Büyüköztürk (2020b) proposed a novel implementation of the frequency domain decomposition, together with an optimal task allocation algorithm to maximize the efficiency of wireless sensor networks.

However, dealing with traffic loads in identifying civil infrastructure is not straightforward. Fraser et al. (2010) proposed integrating image and sensor data acquisition gathered to a single computer to achieve accurate time synchronization between the structural vibration response and corresponding traffic loads. A high-speed wireless Internet network was necessary for this purpose due to the considerable amount of data generated in real time. Marulanda et al. (2017) employed moving sensors to identify dense structural features using only a stationary sensing device and a moving one. Although the considerable reduction of sensors allows more efficient data management, the mentioned study is based on the assumption of white noise excitation and piecewise stationary structural response. Goulet and Smith (2013) established that largely redundant instrumentation might hinder the ability to interpret data. Indeed, several authors investigated optimal sensor placement to avoid redundant sensors and find a compromise between monitoring costs and expected identification performance. For example, Zhou et al. (2017) proposed a tool to find the optimal sensor placement using genetic algorithms.

One of the most well-known hardware solutions employed to build smart sensing nodes in scientific literature is the single-board computer (SBD). The Imote2 platform, developed by Intel Research, has been largely used for laboratory tests and then employed for bridge monitoring (Jang et al. 2010; Rice et al. 2010; Spencer et al. 2016).

In order to make this system suitable for SHM applications of civil infrastructure and accessible to users without expertise on TinyOS, several sensor boards have been designed, and a simplified software framework has been developed afterward. In particular, Rice and Spencer (2008) proposed the SHM-A sensor board, which was employed in the monitoring campaign of the 2nd Jindo Bridge (Jang et al. 2010), while Jo et al. (2012) proposed the SHM-H board with a high-sensitivity accelerometer used to perform the decentralized stochastic modal identification of a steel truss. Moreover, a service-oriented toolsuite was developed to allow researchers and engineers to implement SHM applications easily (Rice et al. 2010). More recently, the Xnode was presented by Spencer et al. (2017), which uses a real-time operating system (RTOS) and a high-resolution analog-to-digital converter (ADC) to address some of the limitations of the Imote2 devices emerged from the long-term monitoring experience of the 2nd Jindo Bridge. Furthermore, Sabato et al. (2016) developed the Acceleration Evaluator, a wireless sensor prototype able to detect microvibrations thanks to the implementation of a voltage-to-frequency converter instead of conventional ADC.

Different computing solutions able to generate a higher throughput were also explored to facilitate high-frequency and real-time applications. Liu and Yuan (2008) proposed a dual-controller-based architecture that comprises a field-programmable gate array (FPGA) supporting a much higher sampling rate compared to traditional SBC-based solutions. Cicada et al. (2010) used an FPGA to perform filtering and downsampling operations in a system used for monitoring the San Siro Meazza Stadium in Milan, Italy. This solution guaranteed durability and the possibility of using high-resolution ADC modules. On the other hand, Varadan (2002) proposed using an application-specific integrated circuit (ASIC) to increase durability and processing speed while reducing size.

Whereas several algorithms have low computational complexity, their implementation in digital systems (i.e., microcontrollers, SBCs, and FPGAs) typically employs many computing steps and extensive memory units to store intermediate results in signal processing operations, thus considerably affecting the overall energy performance. Furthermore, ASICs do not offer versatility since they should be programmed for each specific application.

Phase change memory (PCM) has recently emerged as an attractive tool for in-memory computing, which overcomes the conventional computation model by performing operations directly in a memory device (Ielmini and Wong 2018). Concerning industrial ad commercial applications, PCMs are manufactured only for digital storage at the date (Arnaud et al. 2019). However, recent results highlight their potential for edge computing applications (Ielmini and Ambrogio 2020), as their features allow to accelerate the computation of basic operations, thus reducing power consumption and latency (Ou et al. 2020; Pirovano et al. 2004). Specifically, the PCM technology was successfully employed for image recognition implementing machine learning tools (Burr et al. 2015; Joshi et al. 2020; Tuma et al. 2016), and it demonstrated particularly performant for the development of low-power computing architectures (Yoon et al. 2018), as well as hardware accelerators for data-centric frameworks (Narayanan et al. 2021).

To the best of the authors' knowledge, the benefits of PCM technology have never been employed for signal filtering or SHM purposes. In this study, the workflow of a structural identification algorithm recently proposed for applications in the civil field (Quqa et al. 2021a) is adapted for efficient distributed implementation using PCMs. The proposed identification method is mainly based on signal filtering and allows the extraction of both dynamic and quasi-static structural parameters, namely, mode shapes and curvature influence lines of the instrumented structure employing extremely sparse sensor networks. Specifically, an iterative version of the algorithm proposed in (Quqa et al. 2021a) makes filtering particularly suitable for practical implementation in PCM-based smart nodes for civil infrastructure monitoring under traffic loads.

In this study, the proposed algorithm is simulated in a MATLAB environment using the observations collected on a real PCM test unit provided by STMicroelectronics (Carissimi et al. 2019). Besides, the procedure is tested employing vibration data collected using force balance accelerometers deployed on an Italian reinforced concrete viaduct.

In this paper, the next section delineates in detail the workflow of the algorithm, explaining how particular filters can be used for structural identification. Then, the implementation strategy and how PCMs can be effectively programmed to perform filtering operations are explained. Identification results obtained using the vibration response of the case study under vehicular loads are then reported. The use of freshly programmed PCMs is compared to long-term applications to investigate the effects of time-dependent nonidealities of the PCM cells on the identification results. Final remarks conclude the paper.

Structural identification of bridges

Modal parameters are among the most used structural features for the health monitoring of civil infrastructure. Specifically, modal curvature, calculated from identified mode shapes, is at the basis of several damage identification procedures, as it has proven to be particularly effective in detecting localized stiffness reductions (Fan and Qiao 2011). However, major drawbacks of curvature include its rather approximate computation from sparse estimates of the mode shapes and the sensitivity to inaccuracies in identified parameters. A novel integrated approach was recently proposed to identify modal parameters and curvature influence lines using sparse sensor networks (Quqa et al. 2021a). This method is based on filtering raw accelerations collected on the bridge and a simple normalization. This approach has been demonstrated particularly suitable for statically determinate structures, for which it can also provide a quantification of structural damage. As shown in (Quqa et al. 2021a), the acceleration response of a bridge during the passage of a vehicle is formed of quasi-static and dynamic contributions that populate different frequency ranges in the response spectrum. Therefore, it is particularly convenient to study these different contributions independently upon filtering the acceleration response.

Identification algorithm

Consider the impulse responses $b_m[\tau]$, with $\tau = 1, \ldots, N$, of one low-pass ($m = 0$) and p bandpass ($m = 1, \ldots, p$) filters such that the central frequencies of the bandpass filters coincide with the first p resonant frequencies of a vibrating structure and their frequency bandwidth is small compared to the distance between consecutive modal frequencies. Let the coefficients of these filters be organized in column vectors $\mathbf{b}_m \in \mathbb{R}^N$. A filter bank matrix can be defined as follows:

$$\mathbf{B} = \left[\mathbf{b}_0, \mathbf{b}_1, \ldots, \mathbf{b}_p\right] \tag{1}$$

Here, the term $\mathbf{b}_0$ encloses the coefficients of the low-pass filter that can be employed to extract quasi-static structural features. On the other hand, the terms $\mathbf{b}_m$ indicate the bandpass filters used to extract different modal contributions from the acceleration time response (Quqa et al. 2021a). Specifically, considering a matrix $\mathbf{X}_t$ such that

$$\mathbf{X}_t = \left[\mathbf{x}_{t,1}, \mathbf{x}_{t,2}, \ldots, \mathbf{x}_{t,r}\right] \tag{2}$$

where $\mathbf{x}_{t,i}$ are column vectors collecting the samples of the acceleration signal $x_i[t]$ recorded at the instrumented locations $i = 1, \dots, r$ in the time interval $[t, t+N]$, a set of decomposed signals can be calculated as

$$\mathbf{Y}_t = \mathbf{X}_t^{\mathrm{T}}\mathbf{B} = \begin{bmatrix} y_{1,0}[t] & y_{1,1}[t] & \cdots & y_{1,p}[t] \\ y_{2,0}[t] & y_{2,1}[t] & \cdots & y_{2,p}[t] \\ \vdots & \vdots & \ddots & \vdots \\ y_{r,0}[t] & y_{r,1}[t] & \cdots & y_{r,p}[t] \end{bmatrix} \quad (3)$$

The elements $y_{i,0}[t]$, upon changing the time variable into space (i.e., $z = vt$), represent the samples of the curvature influence line of the beam at the i-th location. Due to the Maxwell-Betti reciprocal work theorem, $y_{i,0}[z]$ is also the structural curvature of the beam generated by a static load applied at the i-th instrumented location. Moreover, the terms $y_{i,m}[t]$ with $m = 1, \dots, p$ are the t-th samples of the m-th decoupled modal contributions collected at the i-th location. Therefore, the m-th column vector of $\mathbf{Y}_t$, except when $m = 0$, is an instantaneous (the m-th) mode shape of the instrumented structure.

Based on these concepts, the following identification algorithm is proposed:

1) Collect the structural acceleration response at r instrumented locations when a vehicle is passing on the bridge.
2) Filter each response into $p + 1$ signal components using Equation (3).

3a) For each sensor location, consider $y_{i,0}[t]$ for $t = 1, \dots, T$, where T is the time interval referred to the passage of a single vehicle on the bridge, and normalize this sequence with respect to its maximum value, obtaining

$$h^{(i)}[z]\Big|_{z=vt} = \frac{y_{i,0}[t]}{\max\limits_{t \in [1,T]} y_{i,0}[t]} \quad (4)$$

Equation (4) represents the (normalized) dense influence line of the curvature of the bridge at the i-th instrumented location.

3b) Consider $y_{i,m}[t]$ $(m = 1, \dots, p)$ for $t = 1, \dots, T$ and calculate the mean of the absolute value of the m-th modal amplitude at the i-th location as

$$\phi_{i,m} = \frac{1}{T}\sum_{t=1}^{T}\left|y_{i,m}[t]\right| \quad (5)$$

The vector $\boldsymbol{\phi}_m$ collecting all the $\phi_{i,m}$ for $i = 1, \ldots, r$ is an estimate of the m-th mode shape of the structure, in absolute value.

This procedure is schematized in Figure 1. This implementation is conceived to collect and process short signals acquired during the passage of single vehicles on the monitored bridge span. Traffic load excites the structure considerably, increasing the signal-to-noise ratio of collected structural response, which is typically a challenging aspect when low-cost sensors with a high noise floor and relatively low sensitivity are employed for SHM. Moreover, triggering the acquisition system to collect data only a few times a day during the passage of vehicles, e.g., using the signal collected at the bridge expansion joints (Quqa et al. 2021a), establishes an efficient data collection strategy that could be powered by vibration energy harvesters. The identified parameters can be stored in each sensing node and averaged to the new incomes to improve the robustness to recording noise. Then, the averaged parameters can be transferred to a central unit or directly uploaded to a cloud-based platform at user-defined intervals.

Each node processes the data individually. Moreover, influence lines are calculated locally, without data fusion from multiple instrumented locations. On the other hand, mode shapes are obtained by the ratio of quantities identified at different points. Nevertheless, since phase information (i.e., the sign of the identified modal amplitudes) is neglected, strict synchronization is unnecessary between the sensing nodes. This aspect makes complex and power-consuming synchronization operations avoidable.

While ambient excitation could be employed to identify modal parameters using the presented algorithm, the identification of influence lines needs the passage of a moving load, from which the spatial quasi-static information is retrieved. To date, multiple-vehicle excitation is not supported by the proposed algorithm. Further studies will be conducted on this aspect.

Filter selection

The filters $b_m[\tau]$ should be highly selective in frequency to avoid the mixing of different contributions that would affect the accuracy of the identified structural parameters. In this paper, wavelet filters are employed. The procedure to generate suitable filters for the monitored structure is described herein.

The wavelet packet transform can be implemented using low-pass and high-pass wavelet filters applied recursively n times to the input signal, where n is the selected maximum level of the wavelet transform. This implementation is known as the “Mallat algorithm” or fast wavelet transform (FWT) (Mallat 2009; Quqa et al. 2021b). Specifically, considering a complete decomposition tree, the output coefficients of the wavelet packet transform $d_{i,2k}^{(l)}[t]$ and $d_{i,2k+1}^{(l)}[t]$ obtained by decomposing the coefficients $d_k^{(l-1)}$ at the previous level $(l-1)$ can be calculated as

$$d_{i,2k}^{(l)}[t] = d_k^{(l-1)}[t] * \bar{g}_0[2\tau] \tag{6}$$

$$d_{i,2k+1}^{(l)}[t] = d_k^{(l-1)}[t] * \bar{g}_1[2\tau] \tag{7}$$

where $*$ denotes the convolution operator, $k = 0, \dots, 2^{l-1}$ indicates the subband index of the obtained coefficients, and $g_0[\tau] = \bar{g}_0[-\tau]$ and $g_1[\tau] = \bar{g}_1[-\tau]$ are the impulse responses of the low-pass and high-pass filters associated with a selected wavelet function, respectively. The root of the tree $d_0^{(0)}[t]$ can be assumed coincident with the discrete signal $x_i[t]$ collected at location i if the sampling frequency of the collected signal is sufficiently high – this is known as the “wavelet crime” (Herley 2009). Due to the linearity property of the convolution operator, the decomposition of the signal shown in Equations (6-7) can also be implemented as a one-step (or batch) filtering procedure using 2^n equivalent filters that produce the coefficients at the final transformation level n. These filters can be obtained by cascading (i.e., performing recursive convolution upon upsampling the filter at each iteration) $g_0[t]$ and $g_1[t]$ n times in a particular order (Vetterli and Kovačević 1995). For simplicity, let $G_0(z)$ and $G_1(z)$ be $g_0[t]$ and $g_1[t]$ in the z-transform domain, respectively. Due to the convolution theorem, the frequency representation of an equivalent bandpass filter $b_m[\tau]$ corresponding to the subband $k = m$ at the transform level n can be obtained as

$$B_m(z) = \prod_{l=0}^{n-1} G_{l*}\left(z^{2^l}\right) \tag{8}$$

where $G_{l*}(z)$ can be either $G_0(z)$ or $G_1(z)$ depending on the level l and on the desired equivalent filter. For instance, $G_{l*}(z) = G_0(z)\ \forall l$ to generate the low-pass filter $b_0[\tau]$. In Equation (8), z^k represents an upsampling in the time domain by a factor k, i.e., the upsampled filter $g_{l*}[t]$ at level l can be obtained as

$$g_{l*}[t] = \begin{cases} g_*\left[\frac{t}{2^l}\right] & \text{if } t = h2^l, h \in \mathbb{Z} \\ 0 & \text{otherwise} \end{cases} \tag{9}$$

where $g_*[t]$ is either $g_0[t]$ or $g_1[t]$ depending on the level l and on the desired equivalent filter, and h is an integer value. Consequently, the number of null coefficients of $g_{l*}[t]$ increases with l, while the number of non-zero coefficients is constant.

Each filter obtained through this procedure at level n has a bandpass range width of $F_s/2^{n+1}$, where F_s is the sampling frequency of the collected signal. Applying Equations (6-7) recursively or the equivalent filter obtained through Equation (8) directly to an input signal gives the same outcome, which coincides with the output of the wavelet packet transform at the corresponding frequency range (based on the order of application of the low-pass and high-pass filters), except for a downsampling operation.

In a previous work (Quqa et al. 2021a), the equivalent decomposition filters were obtained by cascading Fejér-Korovkin wavelet filters. In particular, the Fejér-Korovkin 22 wavelet was selected due to its good performance at high decomposition levels, as shown in reference (Quqa et al. 2020). However, these filters have a relatively high number of taps (i.e., 22), which generate equivalent filters that may be particularly challenging for implementations in smart sensing nodes. For instance, considering the wavelet transform level 6, each equivalent filter has 1,326 taps.

In this paper, the reverse biorthogonal wavelet function with three vanishing moments is used for signal decomposition. Specifically, the low-pass and high-pass analysis filters have 4 taps, are symmetrical (anti-symmetrical for the high-pass filter), and are formed of only two coefficients, the higher of which is exactly three times the lower, as shown in Figure 2. Although most equivalent filters obtained through this wavelet function are scarcely selective, the low-pass filter, as well as some bandpass filters, are acceptable for identification purposes, as it will be shown later. In particular, ordering the equivalent filters obtained by cascading the wavelet filters in all the possible orders with an increasing central frequency, the $(2^{n-l}+1)$-th filters are sufficiently selective, especially for low l values (with $l = 1, \dots, n$). These filters have a center frequency equal to

$$F_l = \frac{F_s}{2^{l+1}} \tag{10}$$

Sampling the structural response (i.e., selecting F_s) such that the structural resonant modes have a natural frequency close to the F_l values allows the extraction of the corresponding modal contributions.

Analog in-memory computing strategy

Conventional computing systems employ separate processing and memory units, involving a considerable motion of data, which is expensive in terms of time and energy. This has become a central issue due to the recent growth of highly data-centric applications. In-memory computing overcomes traditional computer architectures, enabling the possibility to perform some tasks in the memory itself and, consequently, avoiding the need to move data between separated processing units (Haensch et al. 2019). Exploiting the physical attributes of dedicated memory arrays, computational tasks are performed within its confines and peripheral circuitry without deciphering the content of the individual memory elements.

PCMs rely on the reversible transition of a chalcogenide material between its crystalline (or SET) and amorphous (or RESET) state. The amorphous phase tends to have low electrical conductance, which reaches values that are several orders of magnitude higher in the crystalline phase. The transition between SET and RESET state is achieved with the application of a corresponding current pulse, which properly modifies the memory cells lattice structure; the SET pulse is a trapezoidal current pulse, which initially melts and then gradually crystalizes the cell phase, producing a cell in a high-conductance state. The SET pulse can be modulated in amplitude, width of the flat portion, and decaying slope. On the opposite, the RESET pulse consists in a higher current flow and it is applied in order to melt the central portion of the cell; the molten material quenches into the amorphous phase, producing a cell in the low-conductance state. The RESET pulse can be modulated in amplitude and width. The order of magnitude of both current pulses amplitude is hundreds of microampere, while their duration could range between tens and hundreds of nanoseconds. Thus, PCMs are already an effective alternative to conventional binary non-volatile memories (NVMs), as in the actual development state, their cells can effectively store digital “0” or “1” values (Burr et al. 2008; Pasotti et al. 2018). These two states correspond to a deep-RESET and a deep-SET state, respectively, and they are achieved through the application of high-amplitude RESET or SET pulse sequences. Furthermore, due to their considerable conductance contrast, the change in read current is quite large, opening up the opportunity for multilevel cell (MLC) operations (Cabrini et al. 2009) due to the intrinsic capability of a memory cell to encode more than one bit of digital data per cell. In other words, PCM cells are able to store a range of intermediate states between the deep-RESET and the deep-SET states. This can be addressed exploting appropriate pulse sequences, called "programming sequence", where the combination of different RESET and SET pulses allows the cells to reach a predefined intermediate conductance. Recent works show the possibility of storing up to 16 different conductance levels per cell (Pedretti and Ielmini 2021). In this context, PCM devices lay among the most appetible enabling technologies for analog in-memory computing. Their aformentioned multilevel storage capability becomes crucial, as it allows the execution of analog multiplications simply exploiting Ohm's and Kirchhoff's laws (Ielmini and Pedretti 2020; Sun et al. 2019). Given a cell with conductance b, a single multiplication is achieved by applying a voltage x to the cell, and thus the readout current I satisfies $I = bx$. If N voltage values are applied to different parallel cells, the sum of their currents y is

$$y = \sum_{\eta=1}^{N} I_\eta = \sum_{\eta=1}^{N} b_\eta x_\eta \tag{11}$$

From this result, it is possible to conceive the whole memory as a conductance matrix **B** with dimensions $M \times N$. Then, applying a voltage vector **x** to each row, it is possible to obtain a matrix-vector multiplication (MVM) as

$$\begin{bmatrix} y_1 \\ \vdots \\ y_M \end{bmatrix} = \begin{bmatrix} b_{11} & \cdots & b_{1N} \\ \vdots & \ddots & \vdots \\ b_{M1} & \cdots & b_{MN} \end{bmatrix} \begin{bmatrix} x_1 \\ \vdots \\ x_N \end{bmatrix} \tag{12}$$

In this study, the elements of **B**, which are in the range of 10-100 µS together with the null value, are proportional to the coefficients of the reverse biorthogonal low-pass and high-pass wavelet filters, whereas the voltage vector **x** contains the sampled input signal, and the current readout **y** represent a sample of the filtered components. Thus, Equation (12) can be seen as the operation to obtain the i-th row of $\mathbf{Y}_t$ in Equation (3), i.e., if **B** is the filter bank matrix, the current readout is the decomposed signal obtained using the PCM-based node deployed at a given instrumented location.

A simplified schematic of the PCM is reported in Figure 3, where the notations used for the conductance values, input voltage, and current readout are expressed in the signal processing format employed in the previous sections. In this representation, the memory array consists of memory cells connected between each other through bitlines (BLs), i.e., the vertical connections, and wordlines (WLs), i.e., the horizontal connections. Each interval $\mathbf{x}_{t,i}$ of the input signal is given as an input to a BL in the form of a voltage $x[t+\eta]$. Therefore, each memory cell connected to a given BL receives the same input voltage. On the other hand, the memory cells connected to a given WL contain the different coefficients of a filter impulse response $b_{\zeta}[\eta]$. The sum of output currents of the memory cells connected to a given WL (i.e., $y_{\zeta}[t]$) constitutes the convolution result between the input signal and the filter stored in the ζ-th WL. Filters that share the same input data can be implemented in the same BLs and different WLs.

It should be noted that the power consumption of an MVM operation is directly proportional to the values of both **x** and **B**, as the total current required to calculate the single elements of **y** is given by Equation 11.

PCM programming

From a practical viewpoint, several challenges characterize the behavior of PCM cells. First of all, low-frequency (flicker) noise affects the values of **B**, as random electron traps are located in the cell lattice. Moreover, cell conductance tends to decrease due to the amorphization and relaxation phenomena of the crystal lattice. Also, different cells respond differently to the same programming pulses, and the response of the same cell to subsequent programming cycles shows a large variability. These phenomena lead to dispersion and inaccuracy of the conductance levels (i.e., to the elements of the **B** matrix) and thus of the MVM operation. Several solutions to mitigate such undesired phenomena have been proposed, mainly focused on material technology (Bruce et al. 2021), post-processing compensations (Joshi et al. 2020; Kersting et al. 2020), or dedicated programming algorithms (Antolini et al. 2021; Braga et al. 2010; Cabrini et al. 2009; Paolino et al. 2021).

In this work, the programming algorithm proposed in (Antolini et al. 2021) has been exploited to store the filter coefficients in an embedded PCM (ePCM) test chip designed and manufactured by STMicroelectronics (Carissimi et al. 2019). The test chip is manufactured in 90-nm smart power Bipolar-CMOS-DMOS technology featuring a specifically optimized Ge-rich Ge-Sb-Te (GST) alloy and was originally intended for digital storage in automotive applications. An evaluation board was also employed and customized in this study, as shown in Figure 4. This board allows the configuration of current pulses applied to cells, exploiting the voltage and current regulators integrated on the test chip. The operations performed on the memory array have been implemented through a dedicated guided user interface (GUI) available on a personal computer. To access the PCM array a high-precision source-meter unit (SMU) has been employed, together with a low-drop power supply.

Upon defining a conductance target interval by specifying its mean value and relative tolerance, each cell is first stimulated with a start SET and a start RESET pulse (Antolini et al. 2021; Zhang et al. 2007), which both have a high amplitude current, as they grant better temporal drift retention (Antolini et al. 2021; Bedeschi et al. 2009). Then, for each cell, an intermediate SET sequence begins with a single minimum SET amplitude A_{MIN}, with the aim of gradually increase the memory element conductance. After a predefined time T_{WAIT}, the cell conductance is measured: if it falls within the target interval, the sequence is terminated, otherwise, if the conductance is lower than the required limit, the cell is stimulated with a new intermediate SET pulse increasing its amplitude by a user-defined interval ΔA. If, instead, the conductance is above the upper limit, the whole process is restarted from the initial SET and RESET pulses. This employed sequence is outlined in Figure 5. The values of A_{MIN}, ΔA and of intermediate SET pulses amplitudes depend on each conductance target and may vary with respect to the programming speed and the accuracy of the algorithm. This iterative procedure is performed since the cell conductance is extremely variable after the application of a pulse. Thereby, it is impossible to predict the conductance value a priori to define a single pulse with suitable amplitude.

In this study, 48 memory cells of a PCM test chip provided by STMicroelectronics were programmed in a laboratory environment to store 24 low and 24 high *rbio3.1* decomposition filter coefficients. The following parameters were used in the described programming algorithm: A_{MIN} = 150 µA, T_{WAIT} = 1 ms, and ΔA = 10 µA. The coefficients of each filter were converted in conductance values $b_{\zeta}[\eta]$, which were then stored into specific memory cells. In particular, low filter coefficients were converted into 18 µS, while high filter coefficients were converted into 54 µS, considering that a scale factor of 2 relates the coefficients of the high-pass and low-pass filter (see Figure 2). The initial conductance value of every filter coefficient was memorized with a maximum tolerable error of ±5%, and the mean number of intermediate steps required to program memory cells was 9.

An effective method for evaluating the above-mentioned long-term effects on PCM cells is to bake the memory array in a thermal chamber for some dozens of hours in order to accelerate the amorphization phenomena of the crystal lattice (Volpe et al. 2019). Recent studies have represented the behavior of PCM cells in time as a power model with the form (Ielmini et al. 2007).

The conductance of the PCM cells was observed using a current source meter unit (SMU) in the laboratory following the time schedule reported in Figure 6. The filter coefficients are collected with a sampling period of 10 min in low sampling frequency (LF) observation intervals, while every 0.02 s in high sampling frequency (HF) intervals. Between LF2 and HF2, the memory array was baked for 48 hours at 150°C to evaluate the effects of time-related nonidealities at an ideal infinite time after programming.

Figure 7 shows the conductance in time of all the monitored cells. Thin lines represent the behavior of individual cells, while the reference power law (Ielmini et al. 2007), fitted to the first two drift intervals, is represented as a thick line for high and low coefficients. According to the power law, the coefficients recorded during the interval LF3 (i.e., after bake and 40 additional days at room temperature) correspond to an equivalent observation time in the order of tens of years since programming. It is therefore assumed that short-term drift effects have completely vanished.

The coefficients observed in the two HF intervals are used to build the 6 low-pass (one for each transformation level) and 4 high-pass (only used in the first four transformation levels) wavelet filters employed in this study to filter the structural vibration response. Each filter is time-dependent due to a noise-related variability, as the stored coefficients are affected by the aforementioned nonidealities.

Recursive procedure for signal decomposition

As explained in the *Filter selection* section, the signal can be decomposed into different wavelet components either using a set of equivalent filters corresponding to a given transformation level (i.e., batch approach) or performing a recursive procedure. The batch approach is represented schematically in Figure 8a-b, and compared to the recursive procedure in Figure 8c-d (the last figure shows only the first two levels of the transform). In this paper, the recursive implementation of the signal decomposition task on the PCM-based architecture is proposed and compared with a batch implementation in terms of power consumption and accuracy of the results. Both algorithms are implemented using real observation of the filter coefficients in PCMs, collected in the laboratory as described in the *PCM programming* section. The structures of the filtering algorithms have been simulated in this study using the MATLAB environment. The input signal, consisting of pre-collected structural vibration data, is sampled and filtered using low-pass and high-pass wavelet filters in a fast wavelet transform implementation – see Equations (6-7) – to retrieve the signal components associated to a wavelet decomposition level equal to n (in this case, $n = 6$). If a batch procedure is adopted, the input samples are decomposed by m (in this case, $m = 4$) equivalent filters whose impulse response is the inverse z-transform of $B_m(z)$ in Equation (8). In this case, the filter bank consists of $N_F = 4$ filters, each with $N_T = 190$ taps. The implementation of this strategy is shown in Figure 8b, where 4 WLs and 190 BLs are required. On the other hand, the recursive implementation is represented in Figure 8c. The filter bank consists of 6 layers, each of them having a different number of filters N_F, ranging from 2 to 4, with an increasing number of taps N_T, ranging from 4 to 97, with an increasing number of null values (Figure 8d). As illustrated in Figure 8d, the coefficients of each filter are implemented in a single WL and different BLs, as every tap must be multiplied with a different value of the input signal. If two or more filters share the same input values (i.e., filters 1 and 2 in this case), they are programmed in different WLs, while sharing the same BLs. Thereby, their outputs are available simultaneously and can be cast to the next filters. Between the two filter layers, a current-to-voltage conversion is processed.

In Table 1, the features of batch and recursive approaches are summarized, together with the number of non-zero coefficients per filter N_{ON}.

The recursive procedure has two principal advantages with respect to the memorization of equivalent filters: (1) it drastically reduces the power consumption of the sensing device, and (2) it reduces the noise effects of non-ideal PCM elements.

The performances in terms of power consumption of batch and recursive implementations have been compared considering the energy required to entirely process a single input sample in both cases, neglecting the cost of current-to-voltage conversion steps. Assuming that the energy is given by $E = \int_0^T x_S I \, dt$, where x_S is the supplied voltage, I is a current and T is the operating time interval, the energy per input sample E' is

$$E' = \int_0^T x_S I \, dt = x_S K \bar{\imath} \tau \qquad (13)$$

where K is the total number of taps to process the sample entirely, $\bar{\iota}$ is the mean cell current, and τ is the time required by the PCM array to compute a single product. As x_S and τ are equal in both implementations, the product $K\bar{\iota}$ is the actual energy benchmark. In the batch implementation, $K = \sum N_F N_T = 760$ and $\bar{\iota}$ = 10.6 μA, whereas in the recursive procedure, K = 1245 and $\bar{\iota}$ = 0.61 μA, thus, the power required by the iterative strategy is only 9.43% of the power required by batch filtering, neglecting, in a first approximation, the contribution of current to voltage conversion circuits. In fact, even if the iterative implementation involves more taps than the batch procedure, the total required current is much lower as, according to Equations (8-9) and Table 1, a large number of coefficients are null, thus involving no current consumption.

In order to compare the performance of batch and recursive implementation, 15 samples of the 4 equivalent filters used in this study have been stored in PCM elements and observed after a 48h baking. Figure 9 compares the observed interval (between tap 50 and 65) of the equivalent filter directly memorized in PCM elements (i.e., using a batch approach, see Figure 8a) with the equivalent filter obtained by convolving the low-pass and high-pass coefficients observed in the interval HF2 according to Figure 8c. Specifically, both for the recursive and batch implementation, the filter observed at 100 different time samples collected every 0.02 s is reported (light green and magenta spreads), together with their average (solid green and magenta lines). It is possible to observe that the coefficients of the filter obtained through recursive implementation are closer to the reference values (i.e., the ideal filter that does not account for the PCM nonidealities), although the spread – that represent the short-term noise – is generally higher. The selective performance of the four filters is observable in the frequency domain: Figure 10 shows the equivalent filters obtained through a recursive implementation before and after baking. As in the previous representation, the filter coefficients observed at 100 different time samples are reported as spread and average lines. Although the spread increases after baking, the selective performance of the filters is comparable.

Results and discussion

This section presents the identification results obtained using the proposed algorithm on the experimental data collected on a viaduct of the Italian A24 motorway. Specifically, dynamic and quasi-static identification results are obtained using filters programmed and observed in the test PCM unit. These results are obtained using the memory cells in freshly programmed and long-term conditions, represented by pre-and post-bake environments (i.e., the observation intervals HF1 and HF2, respectively).

The viaduct, called Temperino (Aloisio et al. 2020a; b; c, 2021), consists of a series of single-span post-tensioned prestressed beams in a simply-supported isostatic configuration. The structure has a 2.3m-high trapezoidal cross-section with two 3.85m-wide lateral cantilevered wings (Figure 11b). Pairs of piers with a hollow cross-section support the bridge spans and are placed at a center distance of about 40m. The deck vibration response was collected using ten biaxial force-balance accelerometers (FBAs) deployed on a single span, as shown in Figure 11a-b. The data, originally sampled with a frequency of 200 Hz, was filtered using a low-pass anti-aliasing filter with a cutoff frequency of 40 Hz.

During the recording interval, a car with a mass of 1750 kg and wheel axles distant 2.85 m, as shown in Figure 11c, excited the bridge by moving several times in the two axial directions of the bridge. The car speed was in a range between 30 and 60 km/h. The accelerometers S1, S5, S6, and S10 are located near the expansion joints. The peaks in vertical acceleration recorded by these devices are used to trigger the acquisition interval during the passage of the car, as explained in (Quqa et al. 2021a). In this paper, individual moving cars have been considered.

Since this study is aimed at investigating the usability of PCMs in structural identification applications, the modal parameters identified using the proposed algorithm and implementation technology will be compared to reference parameters identified using a widely used algorithm for structural identification, namely, the frequency domain decomposition (FDD) (Brincker et al. 2001). Precisely, a traditional centralized application of the FDD is employed using 10 acceleration time histories of 1500 s collected at all the locations shown in Figure 11a-b, subsampled at 50 Hz. This method allows the identification of four vibration modes with natural frequencies $\bar{F}_m$ equal to 2.48 Hz, 5.06 Hz, 7.56 Hz, and 9.01 Hz. Other reference estimates of the same parameters obtained the stochastic subspace identification (SSI) method can be found in (Aloisio et al. 2020b).

In order to identify the mode shapes of the first, second, and fourth modes using the proposed method, the signal is resampled at a frequency of 41.5 Hz. This way, since $\bar{F}_1 \cong F_3$ and $4\bar{F}_1 \cong 2\bar{F}_2 \cong \bar{F}_4$, the filters corresponding to a decomposition level 6, with central frequencies $F_3 = 2.59$ Hz, $F_2 = 5.19$ Hz, and $F_1 = 10.38$ Hz, can be effectively employed to extract the modal contributions associated with the modes 1, 2, and 4, respectively. It should be noted that, in this study, it is assumed that the resonant frequencies of the structure (of a rough estimate of them) are already known, e.g., from previous monitoring campaigns, in order to design the filters for identification. This is a reasonable assumption since preliminary tests are usually performed before designing a monitoring system. A low-pass filter obtained for a decomposition level 5 is also employed to extract the quasi-static response component with a frequency lower than $F_s/2^6 = 0.64\ Hz$.

Figure 12 shows time windows of the filtered signals obtained using the filters observed in the intervals HF1 and HF2 (i.e., in the pre- and post-baking environment), compared to the reference filtered signals obtained using ideal filters that do not include the noise generated by PCM cells. Moreover, Figure 13 shows the error of the filtered signal for each filter. Specifically, nRMSE represents the normalized root mean square error (RMSE). The normalization is obtained by dividing both the reference and the filtered signals by their standard deviation. It is possible to observe that the low-pass filter is generally affected by a higher noise level, and, as expected, the noise increases in the post-bake environment. Moreover, the nRMSE of filter 1 is generally the lowest, denoting a good quality of the extracted first modal contribution, as is also evident in Figure 14.

Although the error in the filtered signal is non-negligible, the mode shapes reconstructed using the extracted modal contributions (Figure 14) are very close to the reference ones – obtained using the traditional FDD – both for the pre- and post-bake environments. In Figure 14, the sign of mode shapes is determined using the sign identified through the preliminary FDD-based identification. The high accuracy is confirmed using the modal assurance criterion (MAC) (Allemang 2003; Brincker and Ventura 2015). Figure 15 shows that values close to 1 are obtained comparing the reference and identified shapes, especially for the first two modes. Since the identification method proposed in this paper provides absolute values of the modal amplitudes, their sign is determined based on the reference identified values.

It should also be noted that, although the central frequencies of the filters do not correspond exactly to the resonant frequencies of the structure, the identification results are in good agreement with the reference parameters. Therefore, the method is also robust to slight variations of the resonant frequencies, e.g., due to varying temperature conditions.

Figure 16 shows the influence lines identified in pre- and post- bake environments. In particular, the average results are obtained considering 24 individual estimates computed during as many vehicle crossings. Although the estimates are visibly affected by noise compared to the reference values, the maxima of the influence lines are in the right location (i.e., with reference to Figure 11a, at the instrumented location, indicated in the top-left corner of each plot). Also, the results obtained in the pre- and post- bake environments are very similar to each other, denoting a good performance of the algorithm for long-term applications. The literature has already shown that, although the noise level can be high in quasi-static parameters, they are generally very sensitive to structural damage (Quqa et al. 2021a). Moreover, considering a larger set of individual estimates, the noise level would decrease.

The results reported in this study are affected by both identification uncertainties (mainly due to recording noise) and PCM nonidealities. This last effect, in particular, slightly affects identified parameters if the filter bank is implemented iteratively. Moreover, given the remarkable power saving of over 90% obtained in a first evaluation, the proposed procedure proves to be particularly convenient and worthy of future developments.

Conclusions

This paper proposes a novel identification procedure of modal and quasi-static structural parameters employing recursive filtering, implemented through phase change memories, that are used for the first time in this research field.

Specifically, this study shows that a recursive implementation improves filter accuracy, also reducing energy consumption. The challenges related to time-dependent nonidealities of PCMs are also investigated. Structural parameters identified in two environments, one representative of a short-term implementation right after programming and one representative of a long-term PCM usage, are comparable in terms of accuracy. In particular, the fundamental mode shape is identified with very good accuracy in both cases. This result demonstrates that the PCM does not necessarily need to be freshly programmed for SHM applications. Therefore, energy-consuming periodic reprogramming can be avoided.

Data Availability

Some or all data, models, or codes that support the findings of this study are available from the corresponding author upon reasonable request.

Acknowledgments

The authors would kindly acknowledge the research group of Prof. Rocco Alaggio and, in particular, Dr. Angelo Aloisio (University of L'Aquila, Italy) for having shared the experimental data of the viaduct. This work was supported in part by the Italian Ministry for Education, University and Research (MIUR) under the program "Dipartimenti di Eccellenza (2018–2022)".

References

Allemang, R. J. (2003). "The modal assurance criterion - Twenty years of use and abuse." *Sound and Vibration*, 37(8), 14–21.

Aloisio, A., Alaggio, R., and Fragiacomo, M. (2020a). "Time-domain identification of the elastic modulus of simply supported box girders under moving loads: Method and full-scale validation." *Engineering Structures*, 215.

Aloisio, A., Alaggio, R., and Fragiacomo, M. (2020b). "Dynamic identification and model updating of full-scale concrete box girders based on the experimental torsional response." *Construction and Building Materials*, 264.

Aloisio, A., Alaggio, R., and Fragiacomo, M. (2021). "Bending Stiffness Identification of Simply Supported Girders using an Instrumented Vehicle: Full Scale Tests, Sensitivity Analysis, and Discussion." *Journal of Bridge Engineering*, 26(1), 04020115.

Aloisio, A., Pasca, D. P., Alaggio, R., and Fragiacomo, M. (2020c). "Bayesian estimate of the elastic modulus of concrete box girders from dynamic identification: a statistical framework for the A24 motorway in Italy." *Structure and Infrastructure Engineering*.

Antolini, A., Scarselli, E. F., Gnudi, A., Carissimi, M., Pasotti, M., Romele, P., and Canegallo, R. (2021). "Characterization and programming algorithm of phase change memory cells for analog in-memory computing." *Materials*, 14(7).

Arnaud, F., Zuliani, P., Reynard, J. P., Gandolfo, A., Disegni, F., Mattavelli, P., Gomiero, E., Samanni, G., Jahan, C., Berthelon, R., Weber, O., Richard, E., Barral, V., Villaret, A., Kohler, S., Grenier, J. C., Ranica, R., Gallon, C., Souhaite, A., Ristoiu, D., Favennec, L., Caubet, V., Delmedico, S., Cherault, N., Beneyton, R., Chouteau, S., Sassoulas, P. O., Vernhet, A., Le Friec, Y., Domengie, F., Scotti, L., Pacelli, D., Ogier, J. L., Boucard, F., Lagrasta, S., Benoit, D., Clement, L., Boivin, P., Ferreira, P., Annunziata, R., and Cappelletti, P. (2019). "Truly Innovative 28nm FDSOI

Technology for Automotive Micro-Controller Applications embedding 16MB Phase Change Memory." *Technical Digest - International Electron Devices Meeting, IEDM*, IEEE, 18.4.1-18.4.4.

Bedeschi, F., Fackenthal, R., Resta, C., Donze, E. M., Jagasivamani, M., Buda, E. C., Pellizzer, F., Chow, D. W., Cabrini, A., Calvi, G. M. A., Faravelli, R., Fantini, A., Torelli, G., Mills, D., Gastaldi, R., and Casagrande, G. (2009). "A bipolar-selected phase change memory featuring multi-level cell storage." *IEEE Journal of Solid-State Circuits*, 44(1), 217–227.

Braga, S., Sanasi, A., Cabrini, A., and Torelli, G. (2010). "Voltage-driven partial-RESET multilevel programming in phase-change memories." *IEEE Transactions on Electron Devices*, 57(10), 2556–2563.

Brincker, R., and Ventura, C. E. (2015). *Introduction to Operational Modal Analysis*. *Introduction to Operational Modal Analysis*, John Wiley and Sons, Ltd.

Brincker, R., Zhang, L., and Andersen, P. (2001). "Modal identification of output-only systems using frequency domain decomposition." *Smart Materials and Structures*, 10(3), 441–445.

Bruce, R. L., Ghazi Sarwat, S., Boybat, I., Cheng, C. W., Kim, W., Nandakumar, S. R., MacKin, C., Philip, T., Liu, Z., Brew, K., Gong, N., Ok, I., Adusumilli, P., Spoon, K., Ambrogio, S., Kersting, B., Bohnstingl, T., Le Gallo, M., Simon, A., Li, N., Saraf, I., Han, J. P., Gignac, L., Papalia, J. M., Yamashita, T., Saulnier, N., Burr, G. W., Tsai, H., Sebastian, A., Narayanan, V., and Brightsky, M. (2021). "Mushroom-Type phase change memory with projection liner: An array-level demonstration of conductance drift and noise mitigation." *IEEE International Reliability Physics Symposium Proceedings*, 2021-March.

Burr, G. W., Kurdi, B. N., Scott, J. C., Lam, C. H., Gopalakrishnan, K., and Shenoy, R. S. (2008). "Overview of candidate device technologies for storage-class memory." *IBM Journal of Research and Development*, 52(4–5), 449–464.

Burr, G. W., Shelby, R. M., Di Nolfo, C., Jang, J. W., Shenoy, R. S., Narayanan, P., Virwani, K., Giacometti, E. U., Kurdi, B., and Hwang, H. (2015). "Experimental demonstration and tolerancing of a large-scale neural network (165,000 synapses), using phase-change memory as the synaptic weight element." *Technical Digest - International Electron Devices Meeting, IEDM*, IEEE, 29.5.1-29.5.4.

Cabrini, A., Braga, S., Manetto, A., and Torelli, G. (2009). "Voltage-driven multilevel programming in phase change memories." *Proceedings of the 2009 IEEE International Workshop on Memory Technology, Design, and Testing, MTDT 2009*, 3–6.

Carissimi, M., Mukherjee, R., Tyagi, V., Disegni, F., Manfre, D., Torti, C., Gallinari, D., Rossi, S., Gambero, A., Brambilla, D., Zuliani, P., Zurla, R., Cabrini, A., Torelli, G., Pasotti, M., Auricchio, C., Calvetti, E., Capecchi, L., Croce, L., Zanchi, S., Rana, V., and Mishra, P. (2019). "2-Mb Embedded Phase Change Memory with 16-ns Read Access Time and 5-Mb/s Write Throughput in 90-nm BCD Technology for Automotive Applications." *ESSCIRC 2019 - IEEE 45th European Solid State Circuits Conference*, 135–138.

Cigada, A., Moschioni, G., Vanali, M., and Caprioli, A. (2010). "The measurement network of the San Siro Meazza Stadium in Milan: Origin and implementation of a new data acquisition strategy for structural health monitoring." *Experimental Techniques*, 34(1), 70–81.

Fan, W., and Qiao, P. (2011). "Vibration-based damage identification methods: A review and comparative study." *Structural Health Monitoring*, 10(1), 83–111.

Fraser, M., Elgamal, A., He, X., and Conte, J. P. (2010). "Sensor Network for Structural Health Monitoring of a Highway Bridge." *Journal of Computing in Civil Engineering*, 24(1), 11–24.

Goulet, J. A., and Smith, I. F. C. (2013). "Performance-Driven Measurement System Design for Structural Identification." *Journal of Computing in Civil Engineering*, 27(4), 427–436.

Hackmann, G., Sun, F., Castaneda, N., Lu, C., and Dyke, S. (2008). "A holistic approach to decentralized structural damage localization using wireless sensor networks." *Proceedings - Real-Time Systems Symposium*, IEEE, 35–46.

Haensch, W., Gokmen, T., and Puri, R. (2019). "The Next Generation of Deep Learning Hardware: Analog Computing." *Proceedings of the IEEE*, 107(1), 108–122.

Herley, C. (2009). *Wavelets and Filter Banks*. SIAM.

Ielmini, D., and Ambrogio, S. (2020). "Emerging neuromorphic devices." *Nanotechnology*, 31(9), 092001.

Ielmini, D., Lacaita, A. L., and Mantegazza, D. (2007). "Recovery and Drift Dynamics of Resistance and Threshold Voltages in Phase-Change Memories." *IEEE Transactions on Electron Devices*, 54(2), 308–315.

Ielmini, D., and Pedretti, G. (2020). "Device and Circuit Architectures for In- Memory Computing." *Advanced Intelligent Systems*, 2(7), 2000040.

Ielmini, D., and Wong, H. S. P. (2018). "In-memory computing with resistive switching devices." *Nature Electronics*, 1(6), 333–343.

Jang, S., Jo, H., Cho, S., Mechitov, K., Rice, J. A., Sim, S. H., Jung, H. J., Yun, C. B., Spencer, B. F., and Agha, G. (2010). "Structural health monitoring of a cable-stayed bridge using smart sensor technology: Deployment and evaluation." *Smart Structures and Systems*, 6(5–6), 439–459.

Jindal, A., and Liu, M. (2012). "Networked computing in wireless sensor networks for structural health monitoring." *IEEE/ACM Transactions on Networking*, IEEE, 20(4), 1203–1216.

Jo, H., Sim, S.-H., Nagayama, T., and Spencer, B. F. (2012). "Development and Application of High-Sensitivity Wireless Smart Sensors for Decentralized Stochastic Modal Identification." *Journal of Engineering Mechanics*, 138(6), 683–694.

Joshi, V., Le Gallo, M., Haefeli, S., Boybat, I., Nandakumar, S. R., Piveteau, C., Dazzi, M., Rajendran, B., Sebastian, A., and Eleftheriou, E. (2020). "Accurate deep neural network inference using computational phase-change memory." *Nature Communications*, 11(1).

Kersting, B., Ovuka, V., Jonnalagadda, V. P., Sousa, M., Bragaglia, V., Sarwat, S. G., Le Gallo, M., Salinga, M., and Sebastian, A. (2020). "State dependence and temporal evolution of resistance in projected phase change memory." *Scientific Reports*, 10(1).

Liu, L., and Yuan, F. G. (2008). "Wireless sensors with dual-controller architecture for active diagnosis in structural health monitoring." *Smart Materials and Structures*, 17(2), 025016.

Long, J., and Büyüköztürk, O. (2020). "A power optimised and reprogrammable system for smart wireless vibration monitoring." *Structural Control and Health Monitoring*, 27(2).

Mallat, S. G. (2009). *A wavelet tour of signal processing*. Academic Press.

Marulanda, J., Caicedo, J. M., and Thomson, P. (2017). "Modal Identification Using Mobile Sensors under Ambient Excitation." *Journal of Computing in Civil Engineering*, 31(2), 04016051.

Narayanan, P., Ambrogio, S., Okazaki, A., Hosokawa, K., Tsai, H., Nomura, A., Yasuda, T., Mackin, C., Lewis, S. C., Friz, A., Ishii, M., Kohda, Y., Mori, H., Spoon, K., Khaddam-Aljameh, R., Saulnier, N., Bergendahl, M., Demarest, J., Brew, K. W., Chan, V., Choi, S., Ok, I., Ahsan, I., Lie, F. L., Haensch, W., Narayanan, V., and Burr, G. W. (2021). "Fully On-Chip MAC at 14 nm Enabled by Accurate Row-Wise Programming of PCM-Based Weights and Parallel Vector-Transport in Duration-Format." *IEEE Transactions on Electron Devices*, 68(12), 6629–6636.

Noel, A. B., Abdaoui, A., Elfouly, T., Ahmed, M. H., Badawy, A., and Shehata, M. S. (2017). "Structural Health Monitoring Using Wireless Sensor Networks: A Comprehensive Survey." *IEEE Communications Surveys and Tutorials*, 19(3), 1403–1423.

Ou, Q. F., Xiong, B. S., Yu, L., Wen, J., Wang, L., and Tong, Y. (2020). "In-memory logic operations and neuromorphic computing in non-volatile random access memory." *Materials*, 13(16).

Paolino, C., Antolini, A., Pareschi, F., Mangia, M., Rovatti, R., Scarselli, E. F., Gnudi, A., Setti, G., Canegallo, R., Carissimi, M., and Pasotti, M. (2021). "Compressed sensing by phase change memories: Coping with encoder non-linearities." *Proceedings - IEEE International Symposium on Circuits and Systems*, 2021-May, 1–5.

Pasotti, M., Zurla, R., Carissimi, M., Auricchio, C., Brambilla, D., Calvetti, E., Capecchi, L., Croce, L., Gallinari, D., Mazzaglia, C., Rana, V., Cabrini, A., and Torelli, G. (2018). “A 32-KB ePCM for Real-Time Data Processing in Automotive and Smart Power Applications.” *IEEE Journal of Solid-State Circuits*, 53(7), 2114–2125.

Pedretti, G., and Ielmini, D. (2021). “In-Memory Computing with Resistive Memory Circuits: Status and Outlook.” *Electronics*, 10(9), 1063.

Pirovano, A., Lacaita, A. L., Pellizzer, F., Kostylev, S. A., Benvenuti, A., and Bez, R. (2004). “Low-field amorphous state resistance and threshold voltage drift in chalcogenide materials.” *IEEE Transactions on Electron Devices*, 51(5), 714–719.

Qu, C.-X., Yi, T.-H., Li, H.-N., and Chen, B. (2018). “Closely spaced modes identification through modified frequency domain decomposition.” *Measurement*, 128, 388–392.

Qu, C., Yi, T., and Li, H. (2019). “Mode identification by eigensystem realization algorithm through virtual frequency response function.” *Structural Control and Health Monitoring*, 26(10).

Qu, C., Yi, T., Yao, X., and Li, H. (2021). “Complex frequency identification using real modal shapes for a structure with proportional damping.” *Computer-Aided Civil and Infrastructure Engineering*, 36(10), 1322–1336.

Quqa, S., Landi, L., and Diotallevi, P. P. (2021a). “Automatic identification of dense damage-sensitive features in civil infrastructure using sparse sensor networks.” *Automation in Construction*, 128, 103740.

Quqa, S., Landi, L., and Paolo Diotallevi, P. (2020). “Instantaneous modal identification under varying structural characteristics: A decentralized algorithm.” *Mechanical Systems and Signal Processing*, Academic Press, 142, 106750.

Quqa, S., Landi, L., and Paolo Diotallevi, P. (2021b). “Modal assurance distribution of multivariate signals for modal identification of time-varying dynamic systems.” *Mechanical Systems and Signal Processing*, 148, 107136.

Rice, J. A., Mechitov, K. A., Sim, S. H., Spencer, B. F., and Agha, G. A. (2011). “Enabling framework for structural health monitoring using smart sensors.” *Structural Control and Health Monitoring*, 18(5), 574–587.

Rice, J. A., Mechitov, K., Sim, S. H., Nagayama, T., Jang, S., Kim, R., Spencer, B. F., Agha, G., and Fujino, Y. (2010). “Flexible smart sensor framework for autonomous structural health monitoring.” *Smart Structures and Systems*, 6(5–6), 423–438.

Rice, J. A., and Spencer, Jr., B. F. (2008). “Structural health monitoring sensor development for the Imote2 platform.” M. Tomizuka, ed., 693234.

Sabato, A., Feng, M. Q., Fukuda, Y., Carni, D. L., and Fortino, G. (2016). “A Novel Wireless Accelerometer Board for Measuring Low-Frequency and Low-Amplitude Structural Vibration.” *IEEE Sensors Journal*, 16(9), 2942–2949.

Sabato, A., Niezrecki, C., and Fortino, G. (2017). "Wireless MEMS-Based Accelerometer Sensor Boards for Structural Vibration Monitoring: A Review." *IEEE Sensors Journal*, 17(2), 226–235.

Sim, S. H., Carbonell-Mrquez, J. F., Spencer, B. F., and Jo, H. (2011). "Decentralized random decrement technique for efficient data aggregation and system identification in wireless smart sensor networks." *Probabilistic Engineering Mechanics*, 26(1), 81–91.

Spencer, B. F., Jo, H., Mechitov, K. A., Li, J., Sim, S. H., Kim, R. E., Cho, S., Linderman, L. E., Moinzadeh, P., Giles, R. K., and Agha, G. (2016). "Recent advances in wireless smart sensors for multi-scale monitoring and control of civil infrastructure." *Journal of Civil Structural Health Monitoring*, 6(1), 17–41.

Spencer, B. F., Park, J. W., Mechitov, K. A., Jo, H., and Agha, G. (2017). "Next Generation Wireless Smart Sensors Toward Sustainable Civil Infrastructure." *Procedia Engineering*, 171, 5–13.

Sun, Z., Pedretti, G., Ambrosi, E., Bricalli, A., Wang, W., and Ielmini, D. (2019). "Solving matrix equations in one step with cross-point resistive arrays." *Proceedings of the National Academy of Sciences of the United States of America*, 116(10), 4123–4128.

Tan, J.-S., Elbaz, K., Wang, Z.-F., Shen, J. S., and Chen, J. (2020). "Lessons Learnt from Bridge Collapse: A View of Sustainable Management." *Sustainability*, 12(3), 1205.

Tuma, T., Pantazi, A., Le Gallo, M., Sebastian, A., and Eleftheriou, E. (2016). "Stochastic phase-change neurons." *Nature Nanotechnology*, 11(8), 693–699.

Varadan, V. K. (2002). "Wireless microsensors for health monitoring of structures." *Smart Structures, Devices, and Systems*, E. C. Harvey, D. Abbott, and V. K. Varadan, eds., 526.

Vetterli, M., and Kovačević, J. (1995). *Wavelets and Subband Coding*. Prentice-hall.

Volpe, F. G., Cabrini, A., Pasotti, M., and Torelli, G. (2019). "Drift induced rigid current shift in Ge-Rich GST phase change memories in low resistance state." *2019 26th IEEE International Conference on Electronics, Circuits and Systems, ICECS 2019*, 418–421.

Yi, T.-H., Yao, X.-J., Qu, C.-X., and Li, H.-N. (2019). "Clustering Number Determination for Sparse Component Analysis during Output-Only Modal Identification." *Journal of Engineering Mechanics*, 145(1), 04018122.

Yoon, S. K., Yun, J., Kim, J. G., and Kim, S. D. (2018). "Self-Adaptive Filtering Algorithm with PCM-Based Memory Storage System." *ACM Transactions on Embedded Computing Systems*, 17(3), 1–23.

Zhang, Y., Feng, J., Zhang, Y., Zhang, Z., Lin, Y., Tang, T., Cai, B., and Chen, B. (2007). "Multi-bit storage in reset process of phase-change Random Access Memory (PRAM)." *Physica Status Solidi - Rapid Research Letters*, 1(1).

Zhou, K., Wu, Z. Y., Yi, X. H., Zhu, D. P., Narayan, R., and Zhao, J. (2017). “Generic Framework of Sensor Placement Optimization for Structural Health Modeling.” *Journal of Computing in Civil Engineering*, 31(4), 04017018.

Zonta, D., Glisic, B., and Adriaenssens, S. (2014). “Value of information: Impact of monitoring on decision-making.” *Structural Control and Health Monitoring*, 21(7), 1043–1056.

Table 1. Parameters of the batch and iterative filter banks

FILTER BANK	LAYER	N_T	N_F	N_{ON}
Batch	I	190	4	190
Iterative	I	4	2	4
	II	7	3	4
	III	13	4	4
	IV	25	4	4
	V	49	4	4
	VI	97	4	4

Figure 1

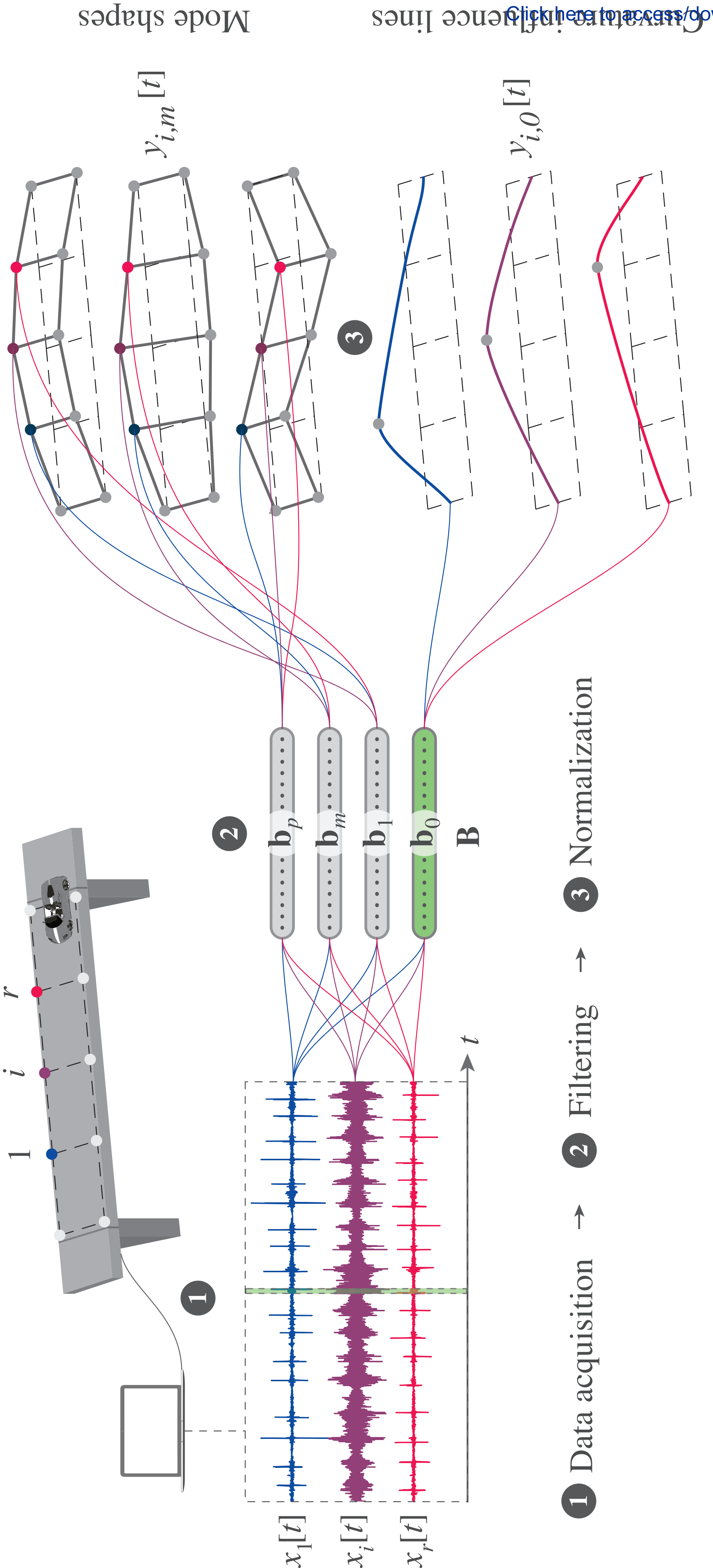

Mode shapes
Curvature influence lines
$y_{i,m}[t]$
$y_{i,0}[t]$
1
i
r
$\mathbf{b}_p$
$\mathbf{b}_m$
$\mathbf{b}_1$
$\mathbf{b}_0$
$\mathbf{B}$
$x_1[t]$
$x_i[t]$
$x_r[t]$
t
1 Data acquisition → 2 Filtering → 3 Normalization

Figure 2

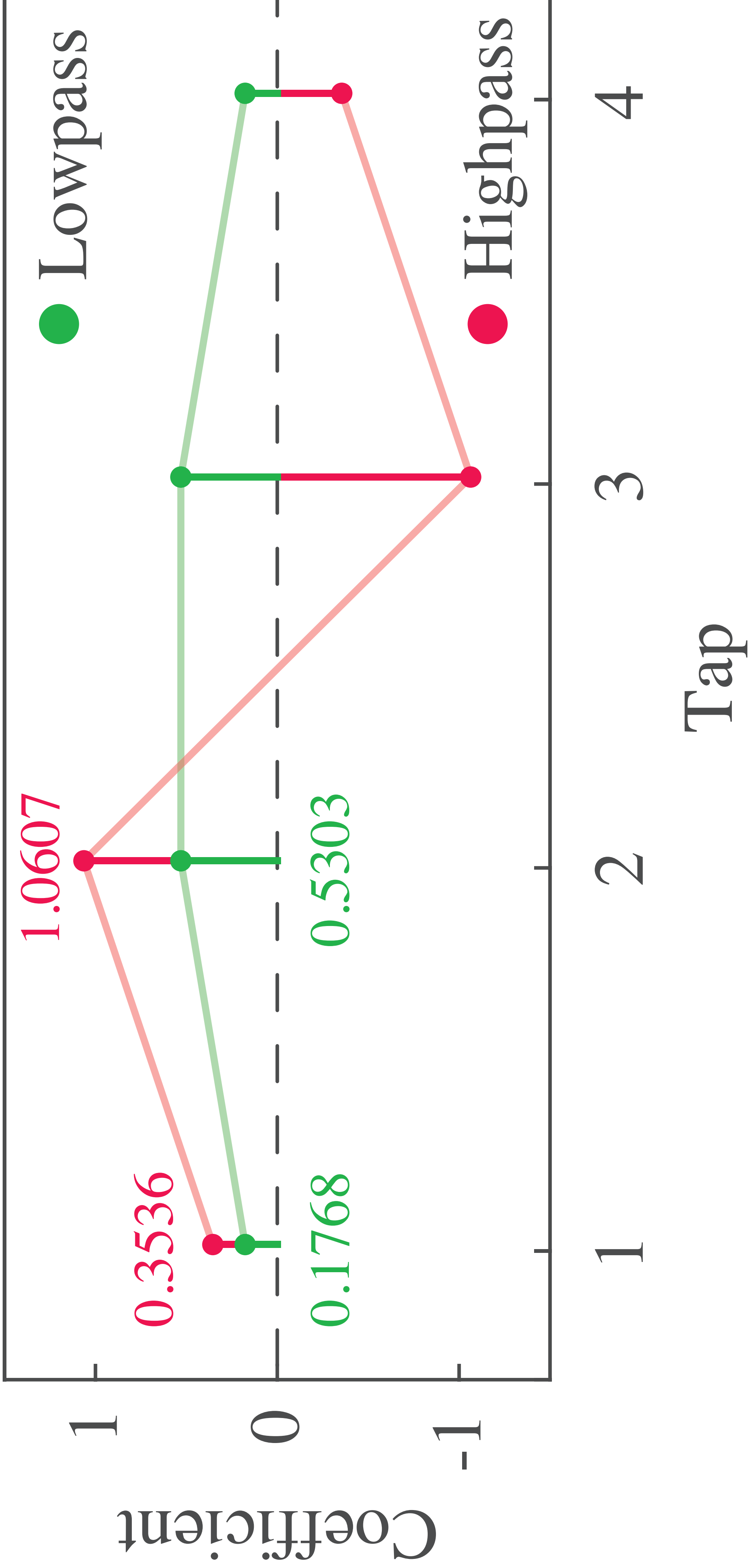

Lowpass
Highpass
1.0607
0.5303
0.3536
0.1768
1
0
-1
Coefficient
1
2
3
4
Tap

Figure 3

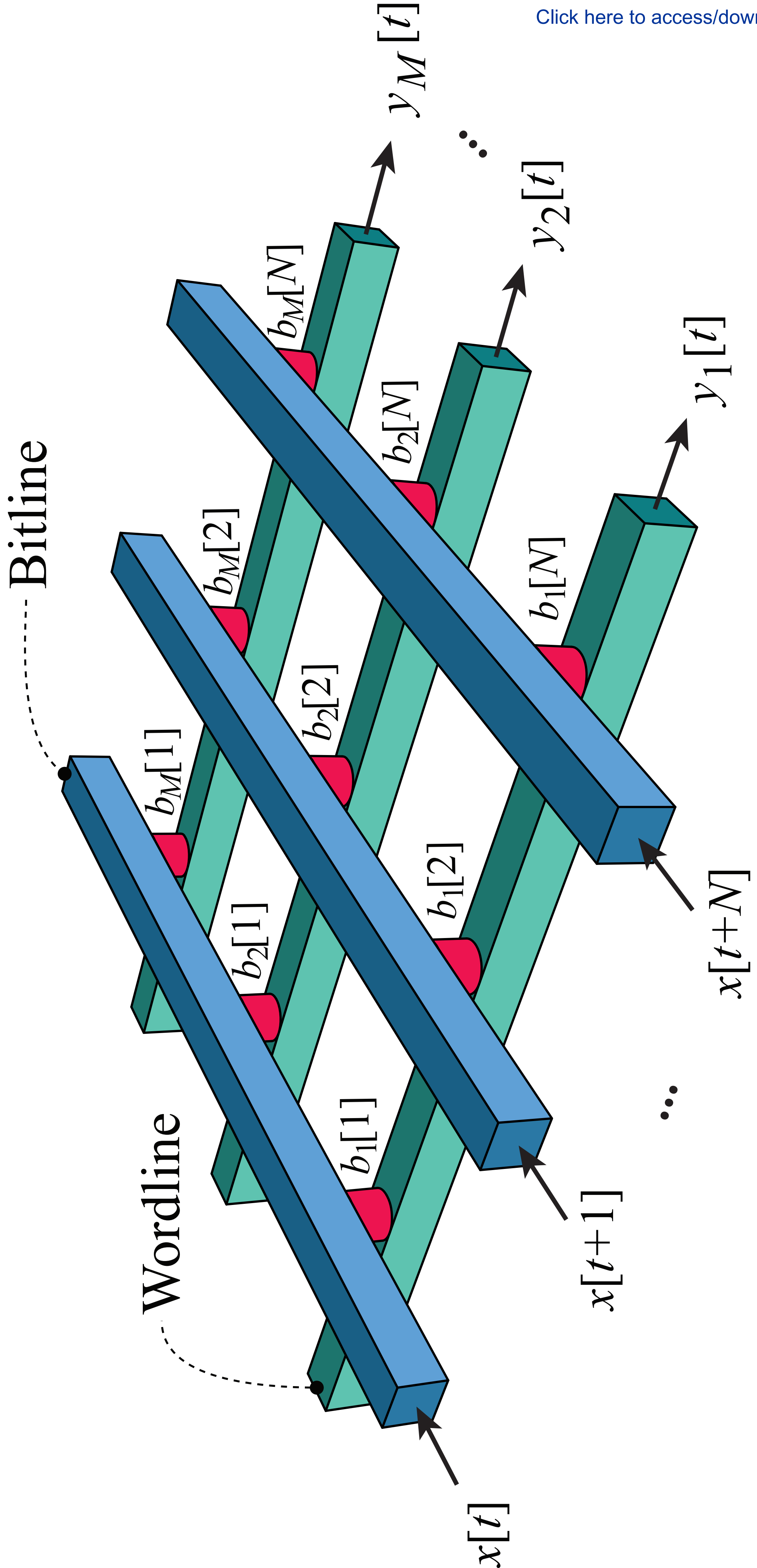

Bitline
Wordline
$y_M[t]$
$y_2[t]$
$y_1[t]$
$b_M[N]$
$b_2[N]$
$b_1[N]$
$b_M[2]$
$b_2[2]$
$b_1[2]$
$b_M[1]$
$b_2[1]$
$b_1[1]$
$x[t]$
$x[t+1]$
$x[t+N]$

Figure 4

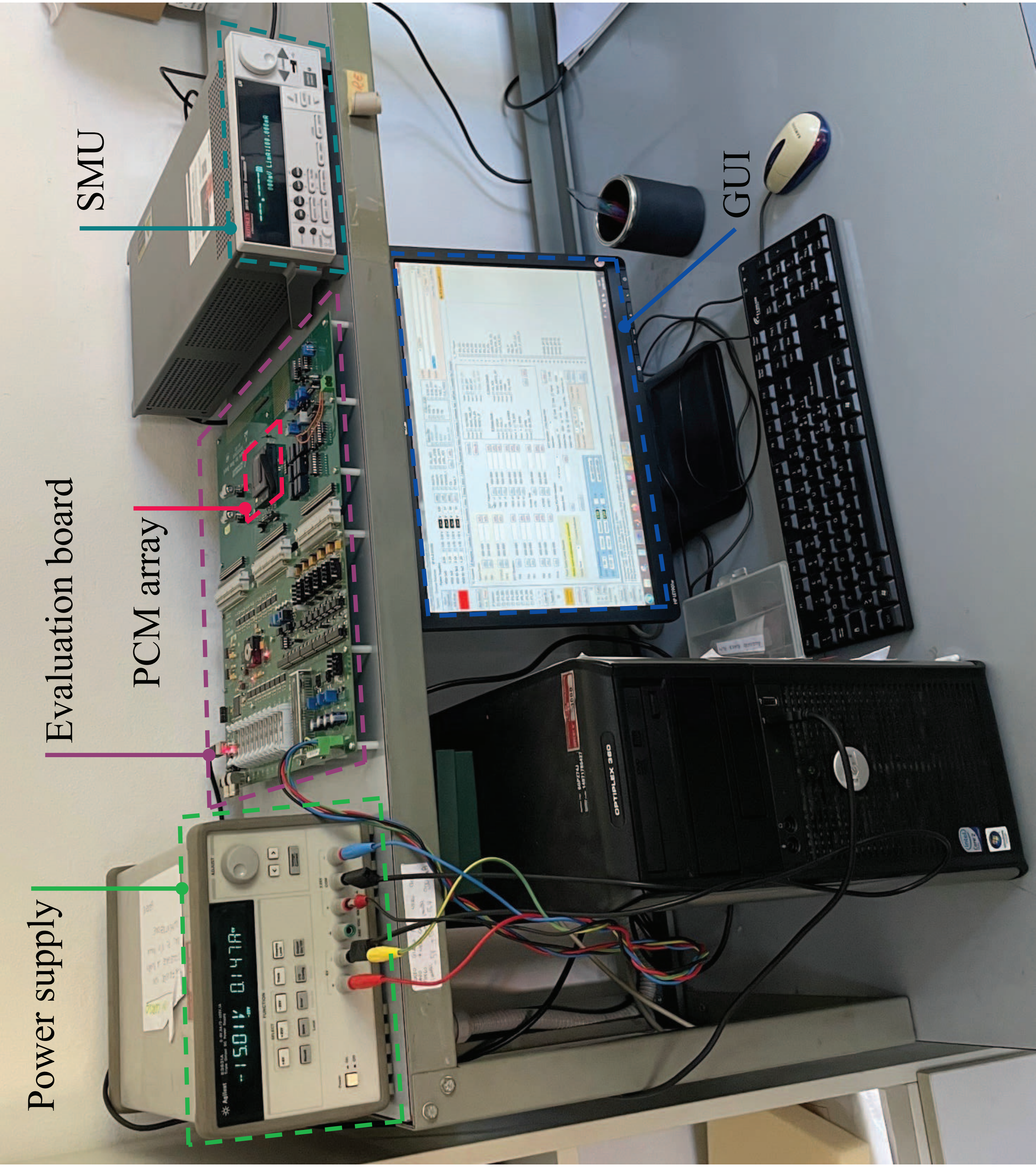

Figure 5

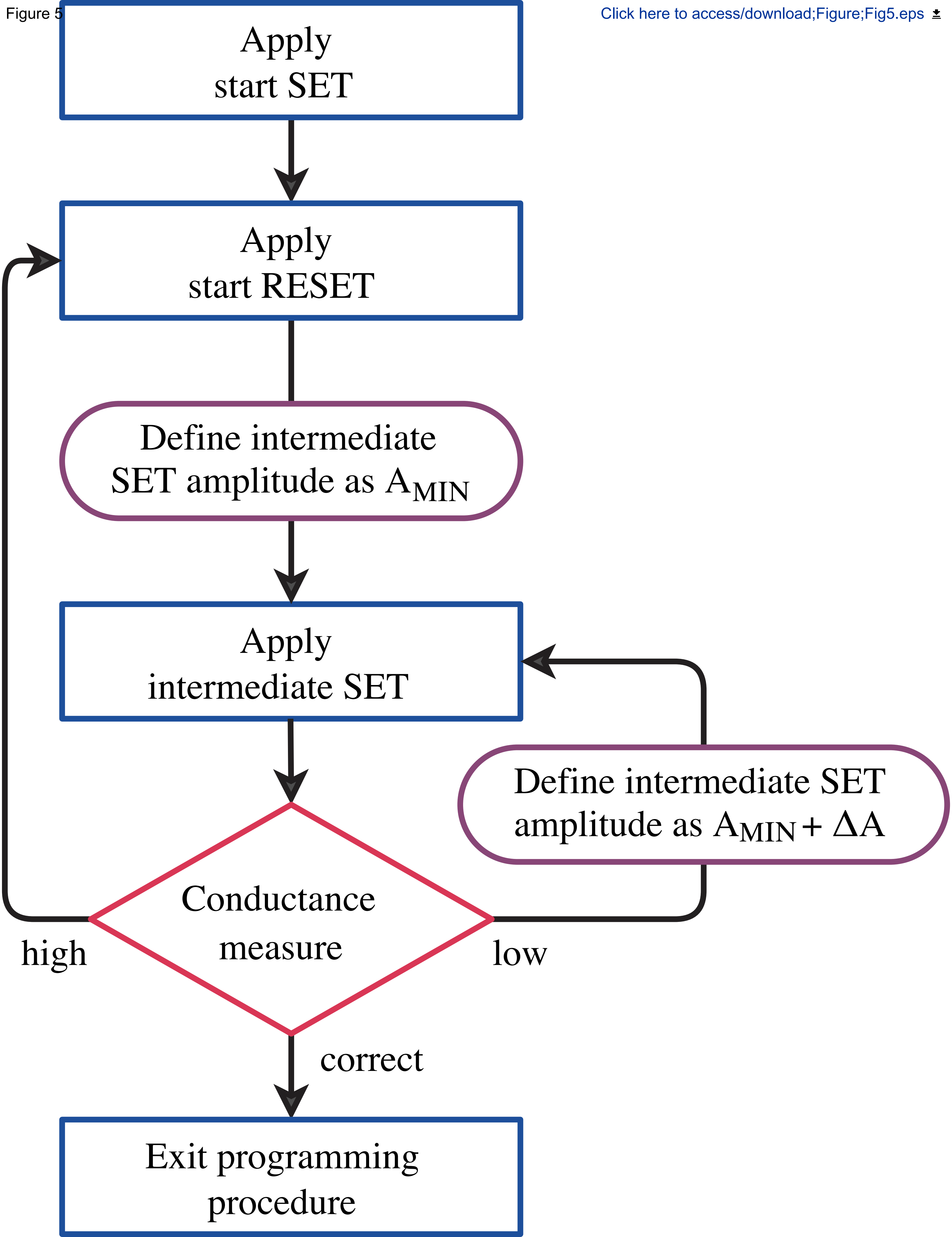
Apply
start SET
Apply
start RESET
Define intermediate
SET amplitude as A_{MIN}
Apply
intermediate SET
Define intermediate SET
amplitude as $A_{MIN} + \Delta A$
Conductance
measure
high
low
correct
Exit programming
procedure

Figure 6

Click here to access/download;Figure;Fig6.eps

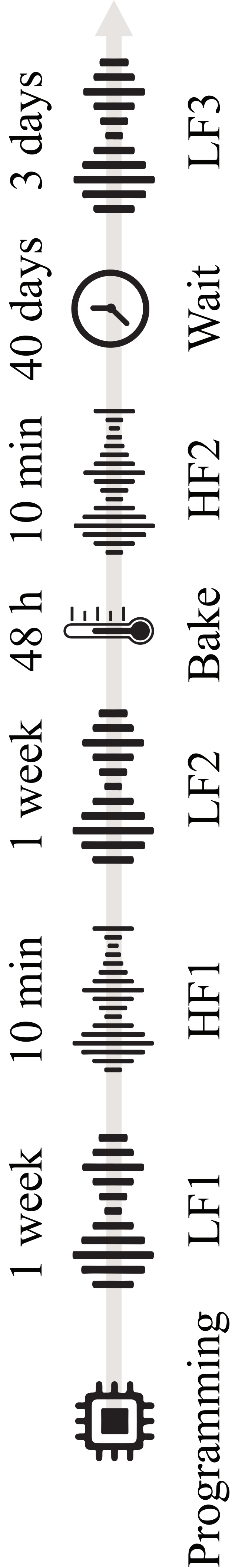

Figure 7 Click here to access/download;Figure;Fig7.eps

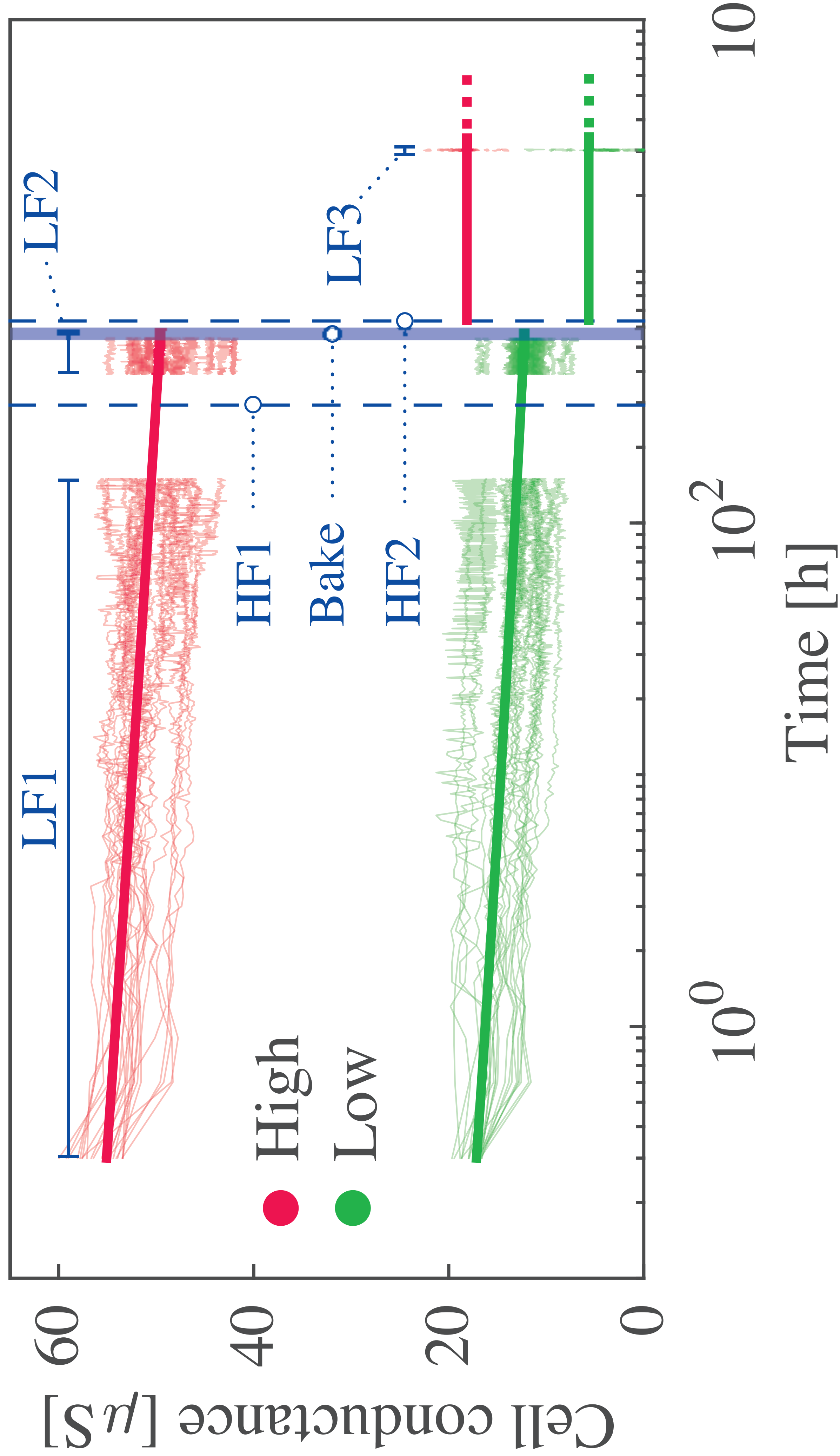

Figure 8

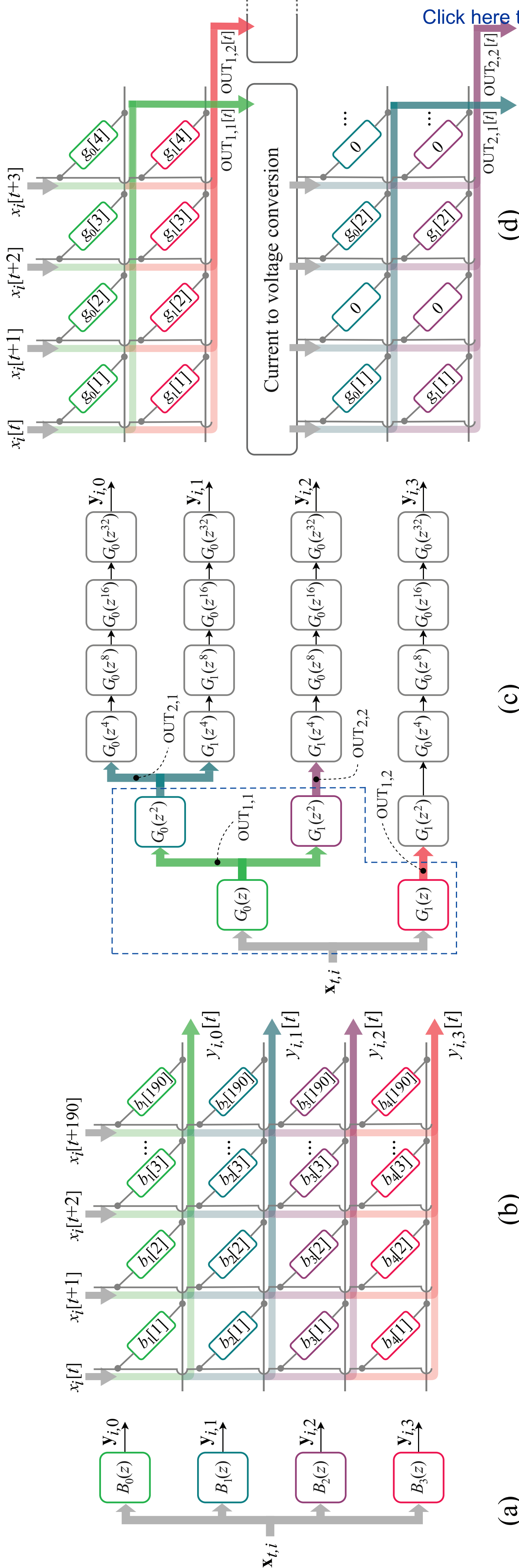

Figure 9

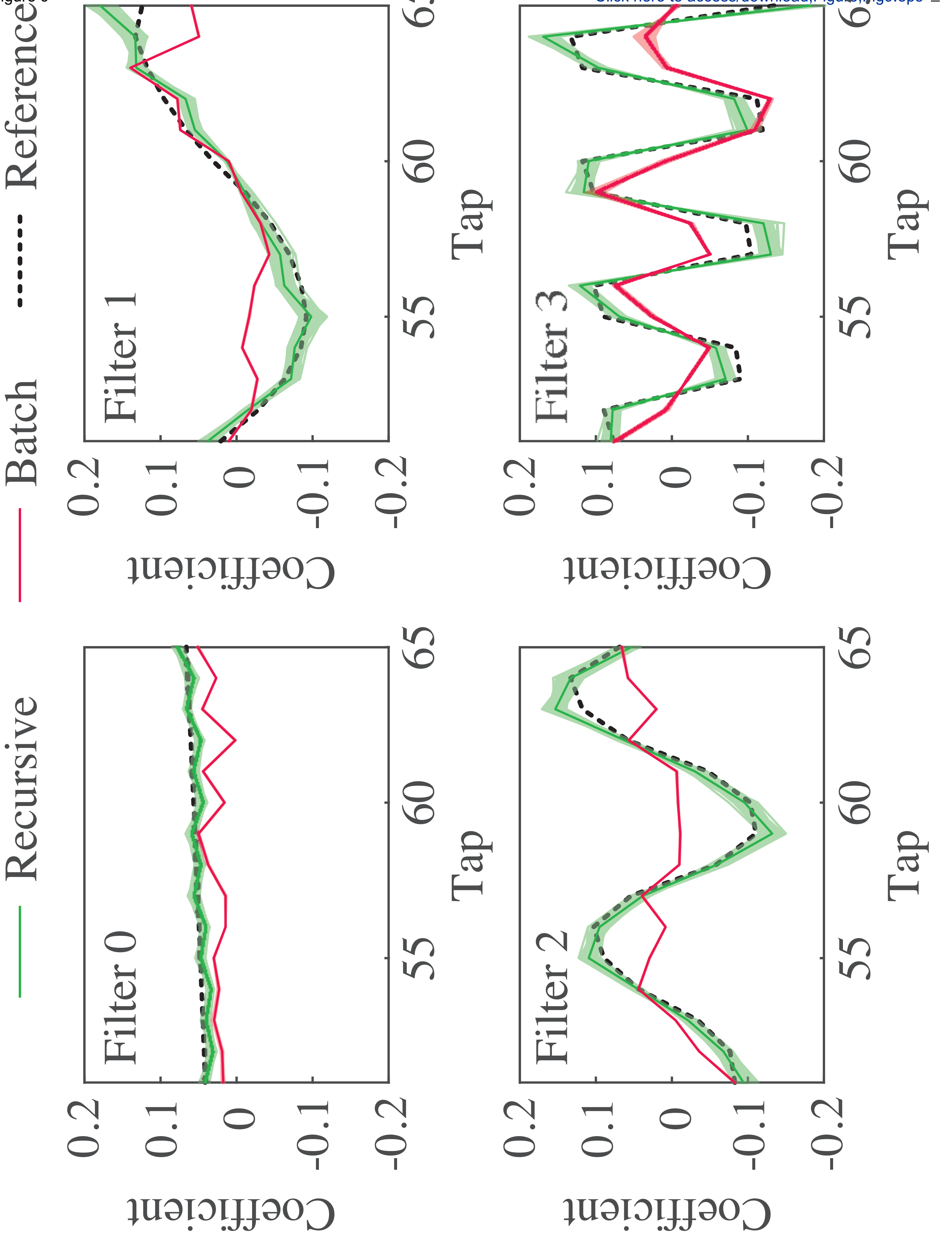
Recursive
Batch
Reference
Filter 0
Filter 1
Filter 2
Filter 3
Coefficient
Tap
0.2
0.1
0
-0.1
-0.2
55
60
65

Figure 10

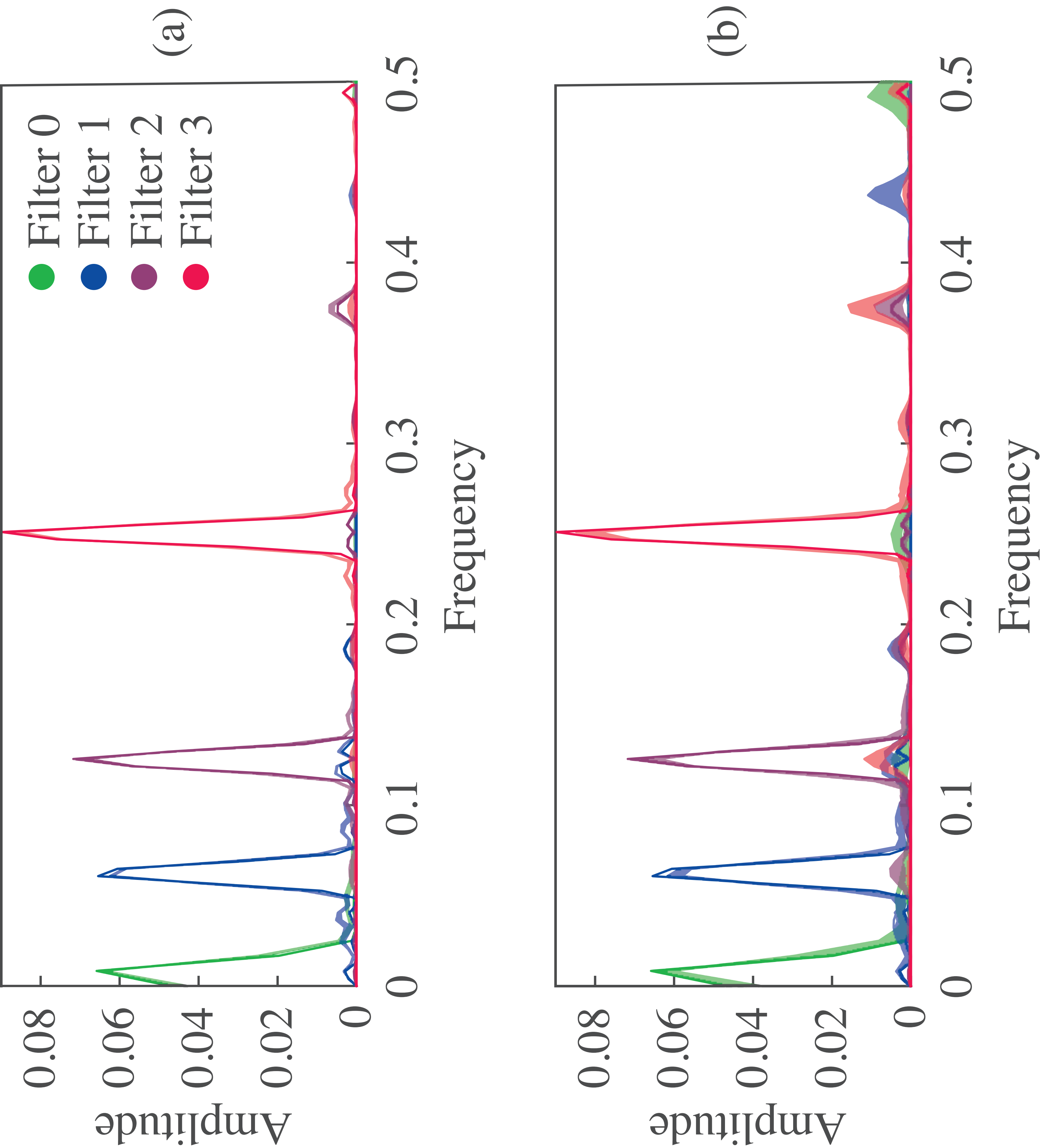
(a)
Filter 0
Filter 1
Filter 2
Filter 3
Amplitude
0.08
0.06
0.04
0.02
0
Frequency
0
0.1
0.2
0.3
0.4
0.5
(b)
Amplitude
0.08
0.06
0.04
0.02
0
Frequency
0
0.1
0.2
0.3
0.4
0.5

Figure 11

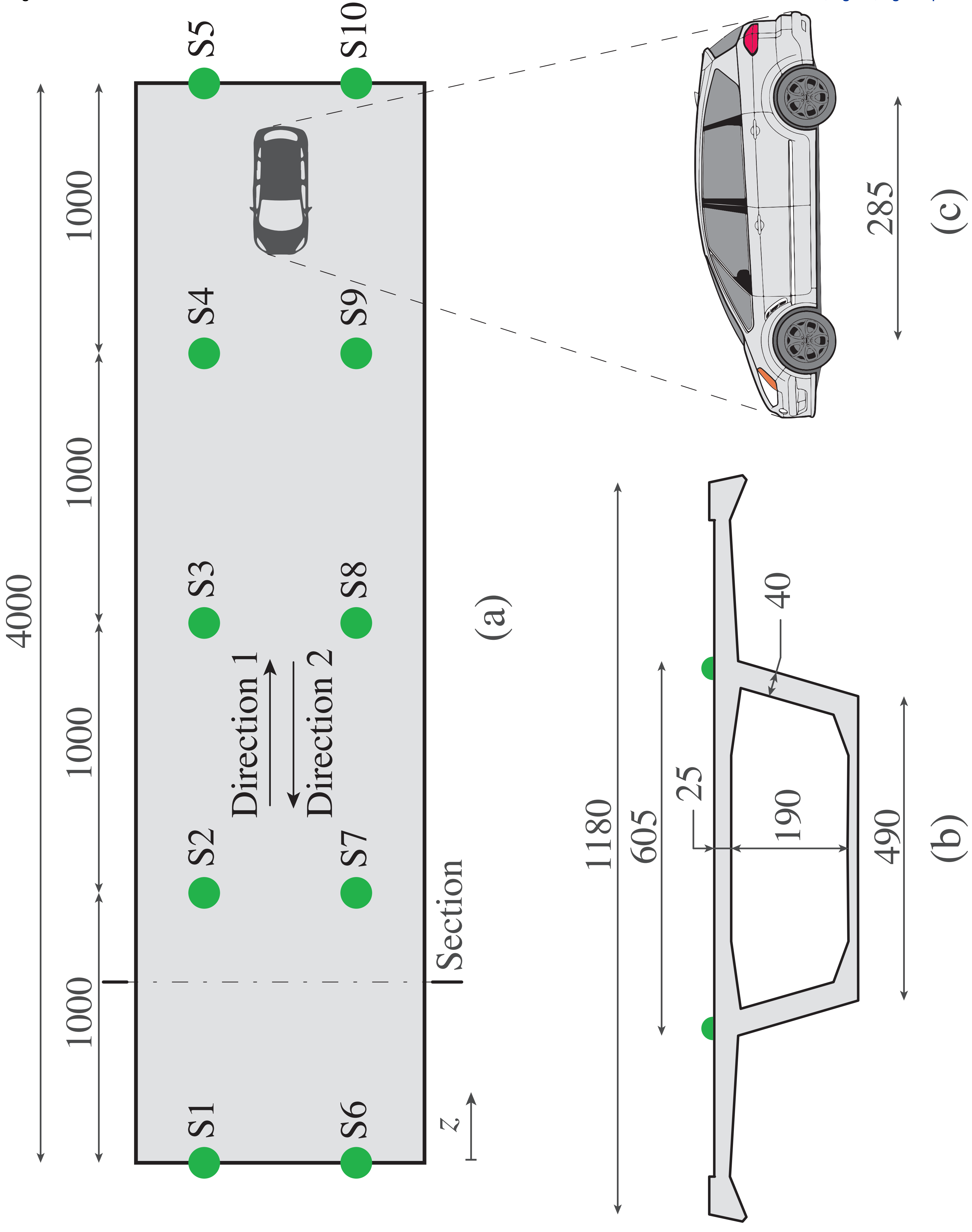
S1
S2
S3
S4
S5
S6
S7
S8
S9
S10
4000
1000
1000
1000
1000
Direction 1
Direction 2
Section
z
(a)
1180
605
25
190
40
490
(b)
285
(c)

Figure 12

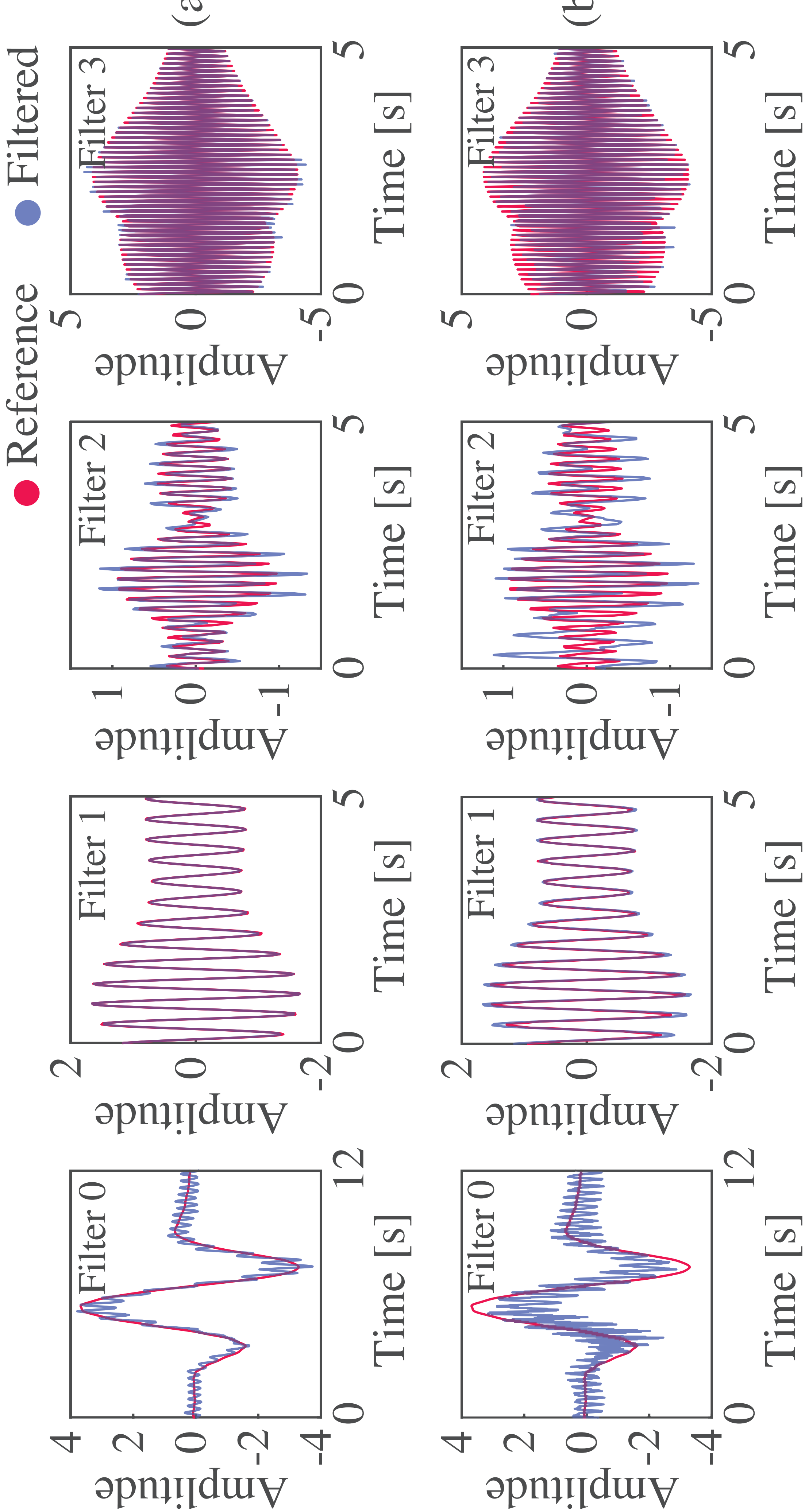

(a)
(b)
Reference
Filtered
Filter 0
Filter 1
Filter 2
Filter 3
Amplitude
Time [s]

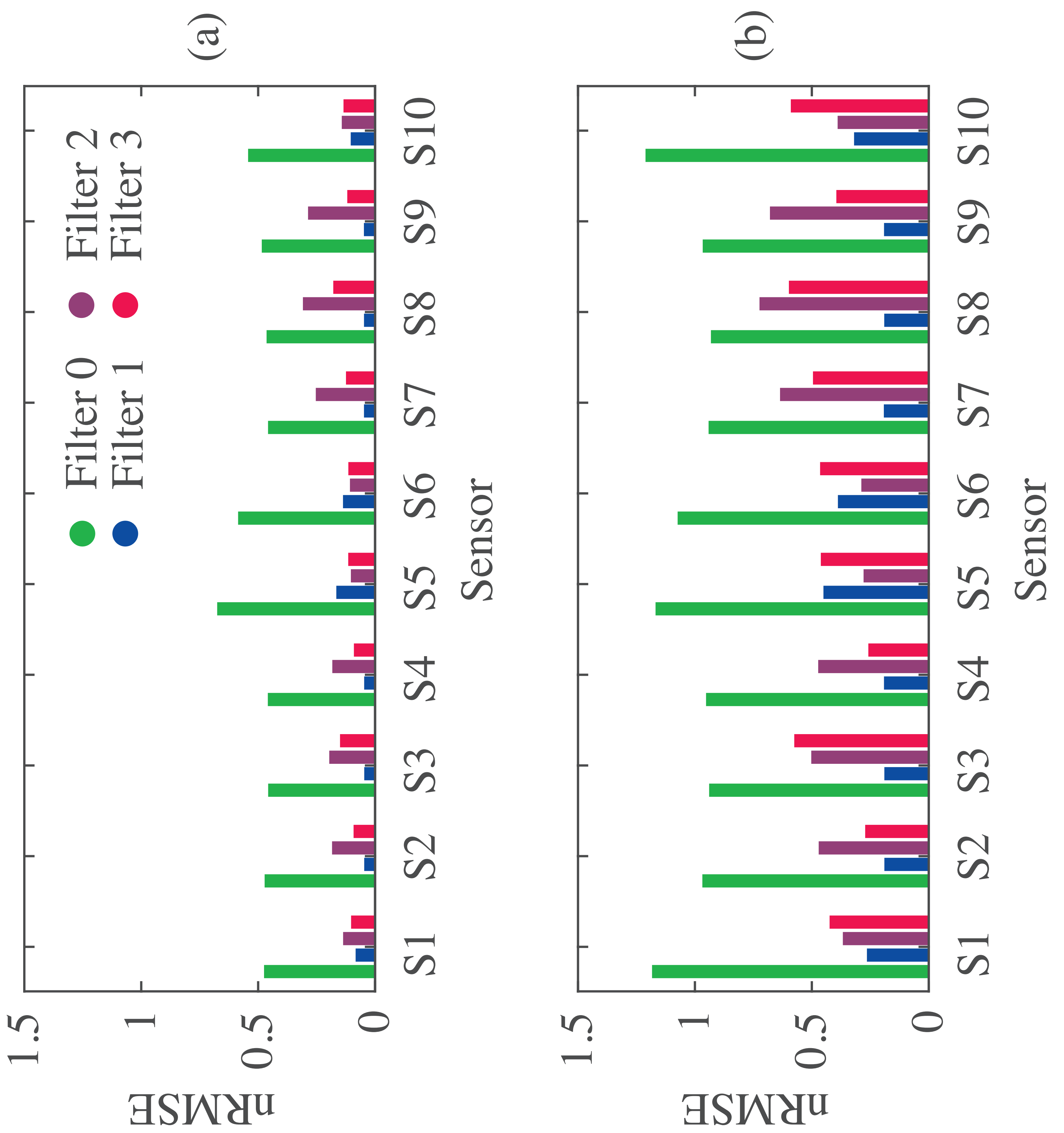
(a)
(b)
Filter 0
Filter 1
Filter 2
Filter 3
nRMSE
Sensor
S1
S2
S3
S4
S5
S6
S7
S8
S9
S10
0
0.5
1
1.5

Figure 14

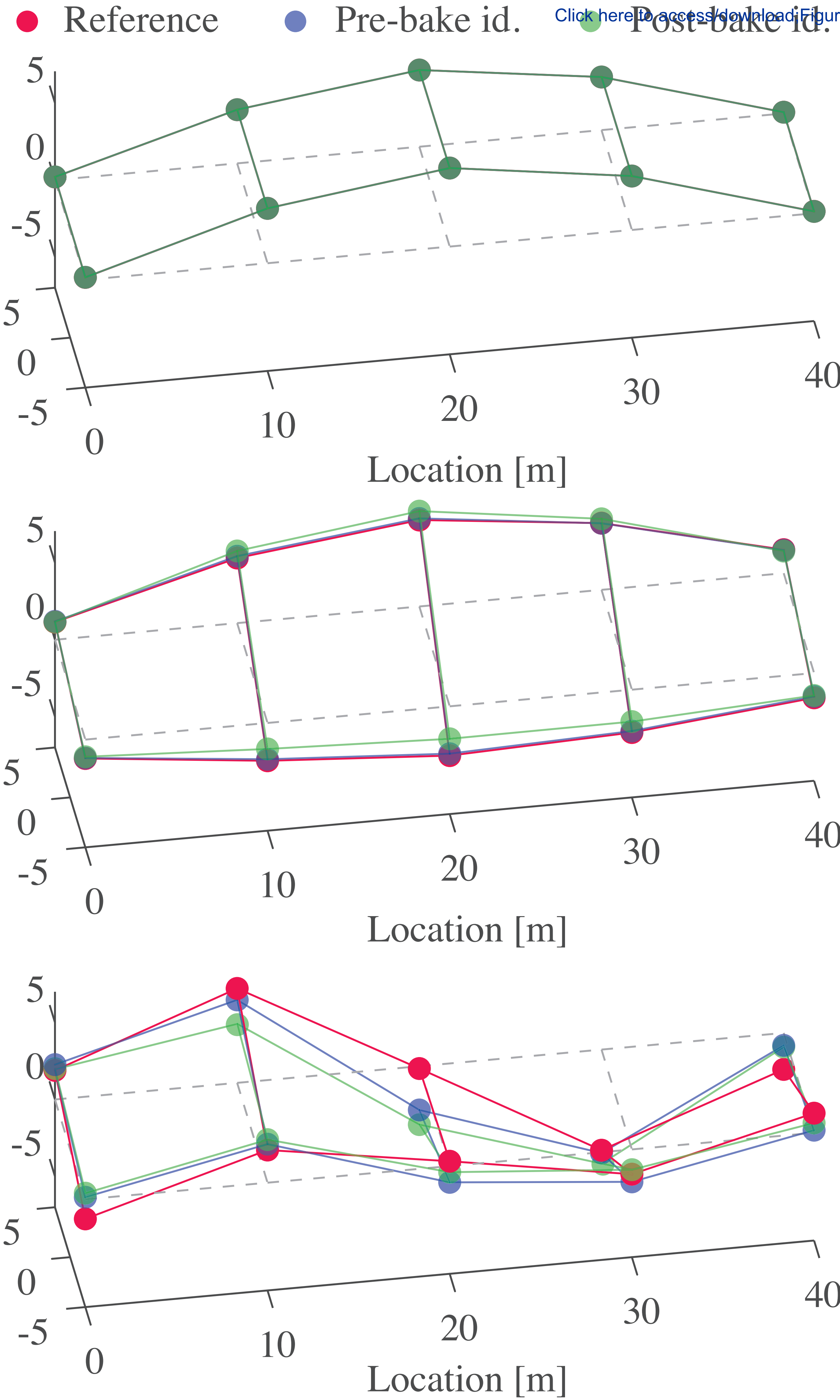
Reference
Pre-bake id.
Post-bake id.
5
0
-5
5
0
-5
0
10
20
30
40
Location [m]
5
0
-5
5
0
-5
0
10
20
30
40
Location [m]
5
0
-5
5
0
-5
0
10
20
30
40
Location [m]

Figure 15

Click here to access/download;Figure;Fig15.eps

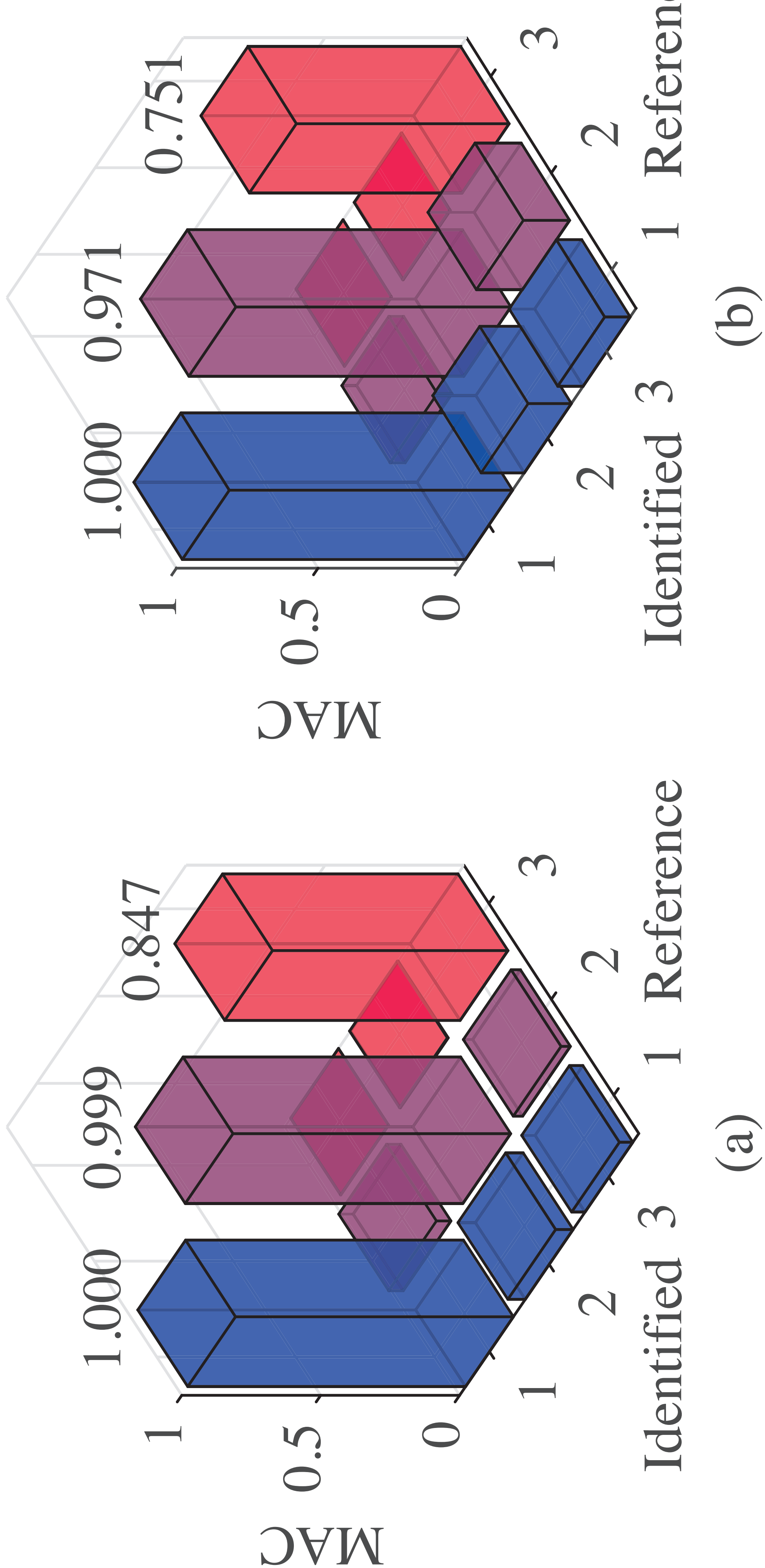

Figure 16

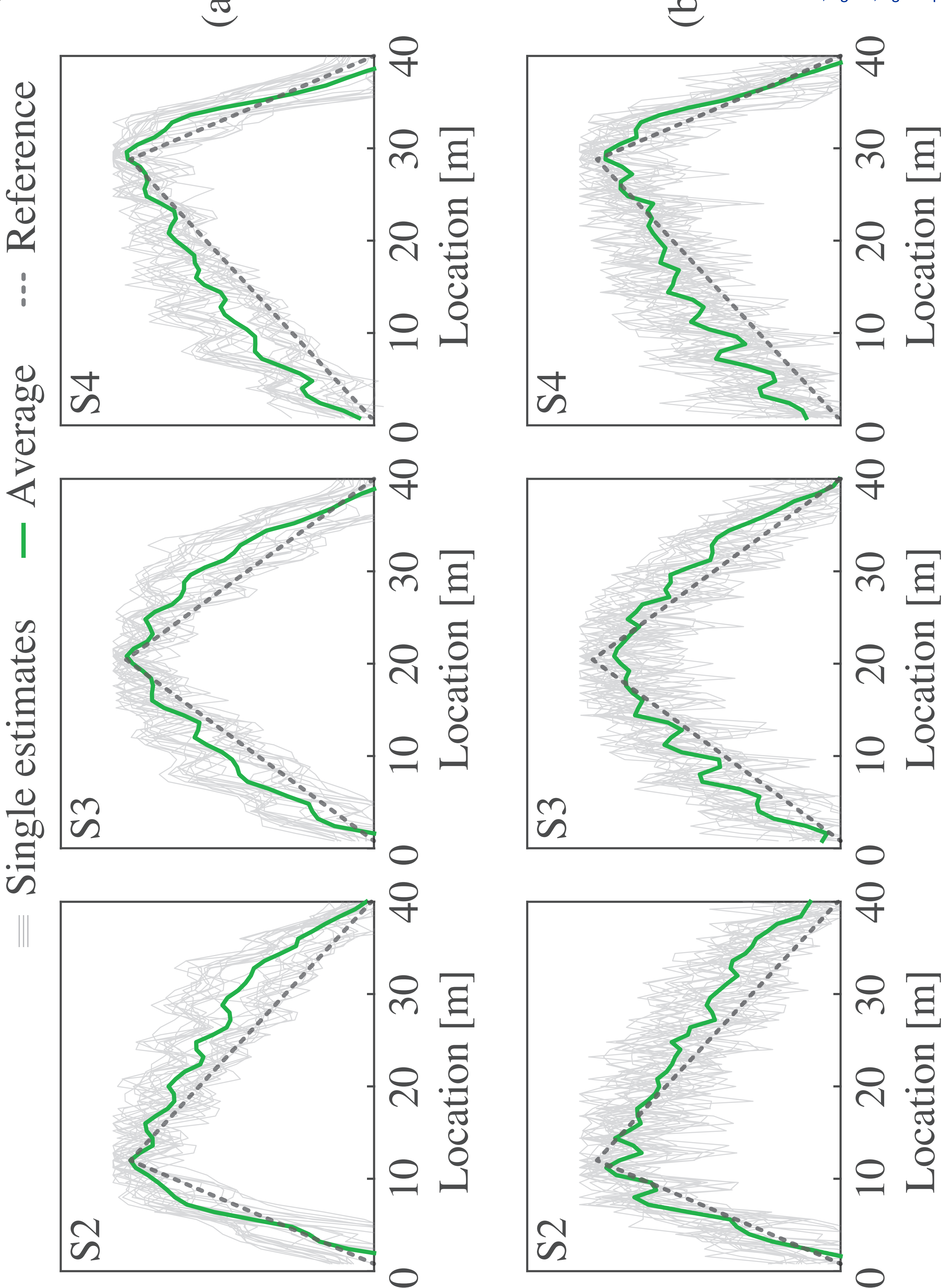
Single estimates
Average
Reference
(a)
(b)
S2
S3
S4
0
10
20
30
40
Location [m]

List of captions

Figure 1. Scheme of the identification algorithm

Figure 2. Reverse biortogonal 3.1 wavelet decomposition filters

Figure 3. Schematics of the PCM array

Figure 4. Laboratory setup for PCM testing

Figure 5. Programming algorithm of the PCM cells

Figure 6. Observation schedule of programmed filters

Figure 7. Drift of the programmed PCM cells

Figure 8. Filtering through the batch (a) and recursive (c) modes, and their respective implementation in a PCM-based architecture (b,d); in (d) the architecture of the dashed portion of (c) is represented

Figure 9. Noise effects on the equivalent filter for a level 6 transform

Figure 10. Selected filters in the frequency domain: pre-bake (a) and post-bake (b) environment

Figure 11. Scheme of the case study

Figure 12. Filtered signals in pre-bake (a) and post-bake (b) environment; filter 0 indicates the low-pass filter, while filters 1, 2, and 3, are band-pass filters with central frequencies F_1, F_2, and F_3, respectively

Figure 13. Normalized root mean square error of the filtered signals in pre-bake (a) and post-bake (b) environment

Figure 14. Reference and identified mode shapes; from top to bottom, output of filters 1, 2, and 3

Figure 15. Modal assurance criterion matrices calculated between identified and reference mode shapes in pre-bake (a) and post-bake (b) environment

Figure 16. Influence lines identified in pre- bake (a) and post-bake (b) environment for different sensor locations